KeAi

CHINESE ROOTS
GLOBAL IMPACT

Contents lists available at ScienceDirect

Petroleum Science





Original Paper

Effects of organic-inorganic transformation and interaction on the occurrence of nanopores within the organic-rich shale during thermal maturation: Insights from the hydrous pyrolysis experiments in a closed system



Yong Tang ^a, Chu-Xiong Li ^{b, c}, Hong Cheng ^a, Su-Yang Cai ^{b, *}, Xiao Li ^a, Qi-Lin Xiao ^{b, **}, Meng-Lin Zheng ^a, Iin Pan ^a

- ^a PetroChina Xinjiang Oilfield Company, Karamay, 834000, Xinjiang, China
- b Key Laboratory of Exploration Technologies for Oil and Gas Resources (Yangtze University), Ministry of Education, Wuhan, 430100, Hubei, China
- ^c Wuxi Research Institute of Petroleum Geology, Sinopec Exploration and Production Research Institute, Wuxi, 214126, Jiangsu, China

ARTICLE INFO

Article history: Received 5 July 2024 Received in revised form 25 November 2024 Accepted 26 February 2025 Available online 28 February 2025

Edited by Jie Hao and Min Li

Keywords:
Shale reservoir
Organic-matter pores
Oil cracking
Organic-inorganic interaction
Clay illitization

ABSTRACT

The organic-inorganic transformation and interaction act as the critical role in the occurrence of nanopores within the organic-rich shales during thermal maturation. Hydrous pyrolysis experiments were conducted on the organic-rich mudrock collected from the Upper Cretaceous Nenjiang Formation of the Songliao Basin, China in a closed system. The pore types and pore network, and organic and inorganic compositions of pyrolyzed shales were detected from the early to over mature stages (% $R_0 = 0.61-4.01$). The experimental results indicate that geochemical transformation of organic matters and minerals and the interaction control the formation and evolution of nanoporosity. In oil window mineral matrix pores are infilled by the generated oil, K-feldspar dissolution by organic acids promotes clay illitization to form illite, and the catalytic effects of clays (e.g. illite) in the complex of organic matter and clays may promote the in-situ retained oil cracking to generate natural gas, resulting in the early occurrence of organic-matter pores in the complex within oil window. Due to significant primary cracking of solid kerogen to generate extractable liquid oil, pore volume for storing fluids presents a persistent increase and approaches the maximum at the end of oil window. In gas window intensive oil cracking facilitates the hydrocarbon migrating out of the source home and pyrobitumen formation, resulting in the significant occurrence of modified mineral matrix pores and organic-matter pores. Pore volume for hosting hydrocarbons presents a slight decrease at %R_o = 1.36-2.47 due to pyrobitumen formation by oil secondary cracking. The organic-inorganic interaction favors clay illitization, quartz dissolution, and pyrite and carbonate decomposition, which facilitate the occurrence of nanoporosity. Pyrobitumen within the complex with illite and organic matters are much more porous than that hosted in modified mineral matrix pores and microfractures. The catalytic effects of clays are supposed to be responsible for this. This study improves our understanding of the formation and evolution pathways of nanoporosity and the underlying controls in organic-rich shales during thermal maturation, and hence should be helpful in evaluating the sweet spots for shale-oil and shale-gas plays in a sedimentary basin. © 2025 The Authors. Publishing services by Elsevier B.V. on behalf of KeAi Communications Co. Ltd. This is an open access article under the CC BY-NC-ND license (http://creativecommons.org/licenses/by-nc-nd/ 4.0/).

E-mail addresses: caisuyang.123@foxmail.com (S.-Y. Cai), qilinxiao@cug.edu.cn (O.-L. Xiao).

1. Introduction

Organic-rich shales in sedimentary basins are not only hydrocarbon sources but also petroleum reservoirs (Jarvie et al., 2007, 2012). The formation and evolution of pore system within shale reservoirs has hence been a critical subject in investigating the unconventional shale-oil and shale-gas systems (Jarvie et al., 2007;

^{*} Corresponding author.

^{**} Corresponding author.

Katz and Arango, 2018). Unlike the conventional clastic and carbonate reservoirs, abundant nanopores are dominated in shale-gas reservoirs, and diagenesis and thermal maturation of organic matter are supposed to have an important effect on the occurrence of nanopores (Loucks et al., 2012; Fabio et al., 2022; Wang et al., 2023).

Mechanical compaction leads to the significant loss of mineral matrix pores, and hence allows organic-matter pores to play the major role in deeply buried shale-gas reservoirs (Loucks et al., 2012; Milliken et al., 2012; Shan et al., 2024). Organic-matter pores can be classified into two types in origins: (I) primary organic-matter pores inherited from the sedimentary organic matter (Mastalerz et al., 2013; Pommer and Milliken, 2015; Sun et al., 2022); (II) secondary organic-matter pores, which are related closely to thermal maturation of organic matter (Jarvie et al., 2007; Mastalerz et al., 2013; Lu et al., 2023; Zheng et al., 2024).

The abundance, type and thermal maturity of organic matters may regulate the formation and evolution of secondary organicmatter pores. TOC is usually correlated positively with pore volumes (Wang et al., 2024). However, this relationship may have a discount at the high TOC level as indicated by the Devonian Marcellus (Milliken et al., 2013) and the Lower Cambrian Niutitang shale gas plays (Wang et al., 2024). The organic matter types also have an effect. Hou et al. (2015) demonstrated that the Type III humic kerogen cannot form abundant organic-matter pores during thermal maturation. Chen et al. (2015) suggested that organicmatter pores in shales with containing Type I kerogen is significantly more abundant (>40 times) than that with type III kerogen. Curtis et al. (2012) have demonstrated the critical role of thermal maturation in forming organic-matter pores. Few organic-matter pores were detected in lower matured samples ($R_0 < 0.90\%$), while abundant organic-matter pores can be observed in highly matured shales (Curtis et al., 2012). This is further confirmed by artificial thermal maturation experiments conducted on organicrich shales (Yang et al., 2018; Ko et al., 2016; Guo et al., 2017; Xiao et al., 2020).

Although the fruitful understanding of forming nanoporosity within shale reservoirs has been achieved, additional experimental work is still needed due to the high variability of nanopores and alterations in nature (Katz and Arango, 2018; Xiao et al., 2020). At present, most published experimental results are extracted from the pyrolysis experiments without water (Chen and Xiao, 2014; Ko et al., 2016; Guo et al., 2017). However, it is well known that water plays an active role in hydrocarbon generation and expulsion (Tannenbaum and Kaplan, 1985a; Lewan, 1997) and mineral transformation (Milliken, 2003), and these processes may have important effects on the occurrence of nanoporosity within shale reservoirs. The recent study has proved that the presence of water facilitates the creation of fractures within pyrobitumen due to the substantial increase in the total pore volume of organic matter in gas window, and the total pore volume is relatively greater for hydrous experiments than those for anhydrous experiments (Liu et al., 2023). More importantly, the interplays between minerals and organic matter on the occurrence of nanoporosity are not yet understood completely, though the minerals play an important role in hydrocarbon generation (Tannenbaum and Kaplan, 1985b; Tannenbaum et al., 1986; Kleber et al., 2021) and oil secondary alteration (Pan et al., 2010; Xiao et al., 2011, 2018). Oil cracking is believed to take place in a relatively closed system (Tissot and Welte, 1984; Hill et al., 2003) and plays a key role in the formation of organic-matter pores (Jarvie et al., 2007, 2012). The catalytic effects of clay minerals can accelerate oil cracking (Pan et al., 2010; He et al., 2022), but its role in forming organic-matter pores is not well understood.

The present study conducted pyrolysis experiments on the organic-rich mudrock from the Upper Cretaceous Nenjiang

Formation of the Songliao Basin (China). A closed hydrous pyrolysis system with the presence of water hence was employed to reconstruct the processes of organic-inorganic transformation and interaction in both oil and gas windows ($%R_0 = 0.61-4.01$), and oil cracking with and without illite at $400\,^{\circ}\text{C}$ for 72 h. This allows us to (1) present a whole map of pore types and pore network evolution; (2) reveal the organic matter and mineral transformation and the interaction; and (3) decipher the possible controls on the occurrence of nanoporosity. It should be useful in improving our understanding of shale-oil and shale-gas reservoir formation and hence the exploration and development in a sedimentary basin.

2. Samples and experimental

2.1. The used shale sample

The used rock sample was collected from the Upper Cretaceous Nenjiang Formation of Well YN7 at the depth of 1802.01 m in the Changling Depression of Songliao Basin, Northeast China. The source rock was deposited in deep lacustrine setting (Jia et al., 2013). It is an organic-rich shale with TOC = 8.16 \pm 0.5 wt%. The low S_1 (4.15 \pm 0.1 mg/g TOC), high S_2 (80.0 \pm 0.8 mg/g TOC), low T_{max} (440 \pm 2 °C) and $\% R_0$ = 0.61 as well as high hydrogen index (HI, 954 mg/g TOC) indicates it is an early matured shale with containing Type I kerogen (Table 1). The mineral composition is dominated by quartz, followed by clays and feldspar, with a little pyrite (Table 1).

2.2. Pyrolysis experiments of shales

The first set of pyrolysis experiments was conducted in 25 mL stainless-steel Hastelloy C-276 reactors with carburized surfaces. 9–16 g bulk rock sample and the same quality of deionized water were loaded into the reactor. In accordance with the calculation based on specific volumes, this ensures the kerogen was submerged in liquid water through the experiment. Before sealing, the reactors were filled with the argon to remove the air. The autoclave was then put into a muffle furnace. Experimental temperatures were kept at 350-600 °C for 12-72 h (Table 1). Temperature and pressure monitoring during the experiment were performed with a type E thermocouple at the standard deviation of ±1.0 °C and pressure sensor at the standard deviation of ± 0.1 MPa, respectively. After the reactors were cooled down to room temperature (25 °C), the final pressure was recorded (Xiao et al., 2020). The other set of pyrolysis experiments with the same conditions were also conducted on an immature coal to constrain the thermal maturity levels of organic matter.

2.3. Oil cracking experiments

In order to clarify the effects of illite on organic-matter pore formation, the second set of pyrolysis experiments for oil cracking was conducted on a normal oil with the density of $0.86 \, \mathrm{g/cm^3}$ with the absence and presence of illite. It was collected from the Lishu Depression of Songliao Basin with the absence and presence of illite. The purity of illite was about 93.3% (Xiao et al., 2011). 4 g oil and 4 g illite were used for the experiments. The onset of significant oil cracking usually occurs at $\geq 400 \, ^{\circ}\text{C}$ in the laboratory with Easy% $R_0 \geq 1.5-1.6$ (Hill et al., 2003). Accordingly, the experimental temperature of oil cracking was set to be 400 $^{\circ}\text{C}$ for 72 h with the calculated Easy% $R_0 = 1.75$ (Sweeney and Burnham, 1990). This ensures the formation of sufficient solid pyrobitumen in the reactor for field emission-scanning electron microscope (FE-SEM) observation.

The experimental data of LECO C-S, Rock-Eval pyrolysis, XRD and N_2 adsorption for natural and pyrolyzed shale samples.

12.0 0.004 0.007	12.0 0.004 0.007 13.4 0.009 0.025	12.0 0.004 0.005 13.4 0.009 0.025 9.2 0.040 0.068	12.0 0.004 0.005 13.4 0.009 0.025 9.2 0.040 0.068 9.9 0.049 0.071	12.0 0.004 0.007 13.4 0.009 0.025 92 0.049 0.016 9.9 0.049 0.071 12.0 0.059 0.068	12.0 0.004 0.007 13.4 0.009 0.025 9.2 0.040 0.068 9.9 0.049 0.071 12.0 0.059 0.068 12.9 0.057 0.063	120 0.004 0.007 124 0.009 0.025 92 0.040 0.068 99 0.049 0.071 120 0.059 0.063 129 0.057 0.063 146 0.053 0.056	120 0.004 0.007 134 0.009 0.025 92 0.049 0.078 120 0.059 0.068 129 0.057 0.068 146 0.053 0.056 101 0.055 0.057	12.0 0.004 13.4 0.009 9.2 0.040 9.9 0.049 12.0 0.055 12.9 0.057 14.6 0.053 10.1 0.055 7.7 0.059
	2.2 5.1							
13 1	13 1 12 1	13 1 12 1 14 /	13 1 12 1 14 /	13 1 12 1 14 / 17 /	13 1 12 1 14 / 17 / 12 / 15 /	1 2 4 5 5 5 5 5 5 5 5 5 5 5 5 5 5 5 5 5 5	13 12 14 17 17 18 18 18 18 18 18 18 18 18 18 18 18 18	13 12 14 17 17 18 13 13 14 14 17
					66 66 66 65 62	66 66 66 65 62 59	66 66 66 65 62 59	0 66 119 66 68 66 85 66 94 65 97 62 99 59 59
954	954 769	954 769 303	954 769 303 141	954 769 303 141 62	954 769 303 141 62 27	954 769 303 141 62 27 11	954 769 303 141 62 27 27 26	954 769 303 141 62 27 21 26
								60.84 440 46.16 446 9.29 449 3.35 438 1.44 548 0.59 588 0.59 N/D
1.07 4.15								1.07 4.15 1.04 6.55 0.95 8.59 0.88 5.04 0.79 1.81 0.85 1.22 0.90 0.74 0.68 1.46 0.21 0.35
	7.53 5.89	7.53 5.89 2.03	7.53 5.89 2.03 2.70	7.53 5.89 2.03 2.70 3.46	7.53 5.89 2.03 2.70 3.69	7.53 5.89 2.03 2.70 3.46 3.69 3.53	7.53 5.89 2.03 2.70 3.46 3.69 3.53 4.12	7.53 5.89 2.03 2.70 3.46 3.69 3.20 3.20
	1.33 0.35 1.16 0.36							
	/ / 0.51 8.15 350 16.8 1.06 8.02	/ 0.51 16.8 1.06 12.0 1.36	/ 0.61 16.8 1.06 12.0 1.36 25.2 1.76	7 0.51 16.8 1.06 12.0 1.36 25.2 1.76 12.0 2.09	16.8 1.06 12.0 1.36 25.2 1.76 12.0 2.09 24.0 2.29	16.8 1.06 12.0 1.36 25.2 1.76 12.0 2.09 24.0 2.29 72.0 2.47	16.8 0.51 16.8 1.06 12.0 1.36 25.2 1.76 12.0 2.09 24.0 2.29 72.0 2.47 72.0 3.00	16.8 0.61 12.0 1.36 25.2 1.76 12.0 2.09 24.0 2.29 72.0 2.47 72.0 3.00 24.0 3.67
								YN-2 YN-3 YN-4 YN-5 YN-5 YN-6 YN-7 YN-7 YN-8 SOO YN-9 SOO

Note: R_0 = the reflectance of vitrinite; TOC = total organic carbon; G_{lorg} = inorganic carbon; H_1 = hydrogen index; SE = Soxhlet extraction.

TR-HI = 100 - $H_1/H_1_0 \times 100\%$, where H_1_0 is the hydrogen index for the pyrolyzed samples, and H_1_0 is the hydrogen index for the used original sample; I/S = illite-smectite mixed layers; I/I = no data available.

2.4. Organic geochemistry and petrology

The fresh and pyrolyzed shale samples were dried in oven at 80 °C and then crushed to <200 meshes for LECO C-S and Rock-Eval measurements. Firstly, the crushed samples were run on LECO CS-230 analyzer to get the total C and S; total organic carbon (TOC) can be obtained after the diluted hydrochloric acid was used to eliminate inorganic C. The amount of inorganic C is the difference between the total C and TOC. These samples were then treated with the mixture of dichloromethane and methanol (v:v, 97:3) by using Soxhlet extractor for 72 h to remove the extractable organic matters. After dried in oven, total C and S and TOC were also analyzed by LECO CS-230 analyzer (Xiao et al., 2020).

The Rock-Eval analysis was performed on the Rock-Eval 6 pyrolysis analyzer. About 100 mg powdered sample was used to get the parameters including S_1 , S_2 , T_{max} . HI, OI and transformation ratio based on HI (TR-HI) (Xiao et al., 2020).

The vitrinite reflectance (R_0) analysis was conducted on a 3Y microphotometer. The standard yttrium aluminum garnet with % $R_0 = 0.904$ and cubic zirconia with % $R_0 = 3.11$ were used to do the calibration. At least 50 readings for each sample were recorded at the oil immersion (Xiao et al., 2020).

The organic macerals of original shale sample were observed by using Leica MPV polarizing microscope. The organic macerals were identified by using reflected white light and blue fluorescence with the Leica polarizing microscope at 50X oil immersion (Xiao et al., 2020).

2.5. X-ray diffraction (XRD)

The X-ray diffraction (XRD) was performed on a Bruker D8 Advance X-ray diffractometer to determine the mineral compositions of fresh and pyrolyzed shale samples. The voltage used was 40 kV, the current was 30 mA. The scan was conducted at a speed of 4° /min, and the scanning angle was 3° – 85° (2 θ). The relative content of minerals was calculated by using the main peak area of specific minerals (Xiao et al., 2020). Data acquisition and processing were facilitated by EVA software from Bruker, which performed background subtraction and peak fitting to accurately determine the positions and intensities of the diffraction peaks. To ensure the accuracy and reliability of our results, each sample was subjected to three independent tests, and the average values were calculated to assess the experimental error. The XRD obtained from the samples were compared against the reference patterns from the International Centre for Diffraction Data (ICDD) to identify the mineral phases present. The XRD analysis error is better than ±3%.

2.6. Low pressure nitrogen adsorption

Shale samples were crushed to 60–80 meshes, dried at 110 °C in the oven and degassed under high vacuum conditions (<10 mmHg) for low pressure isotherm analysis. The nitrogen adsorption and desorption isotherms were collected at 77 K (-196 °C) by using Quantachrome's Autosorb-IQ3 analyzer. The relative pressure (P/P_0) ranges from 0.011 to 0.995 with an equilibration time of 10 s. The pore size distribution and pore volumes were calculated using the BJH model (Barrett et al., 1951). Like LECO C-S analysis, these samples were treated with the mixture of dichloromethane and methanol (v:v, 97:3) by using Soxhlet extractor for 72 h to remove the soluble bitumen. The treated samples were used to do the analysis of low-pressure nitrogen adsorption.

2.7. Field emission-scanning electron microscope (FE-SEM)

FE-SEM imaging was conducted on the Hitachi S4800 and the FEI

Helios NanoLab™ 600 systems. The surfaces of shale samples were polished by Ar ion-milling with an accelerating voltage of 3 kV and a milling time of 4 h. Unlike the shale samples, the solid pyrobitumen formed by oil cracking experiments was put on the conductive adhesive to do the FE-SEM imaging directly with no polish by Ar ion-milling. The images can be acquired with secondary electron (SE) and backscattered electron (BSE) modes. Low accelerating voltages (1–5 kV) with working distances of 3–8 mm were used to prevent the sample from beam damage (Xiao et al., 2020).

3. Results

3.1. Pores in the fresh and pyrolyzed shales

The unheated and pyrolyzed shale samples range from the early to over matured stages ($%R_{o}=0.61-4.01$). Pore types and pore network observed by FE-SEM present significant variations with thermal maturity increasing as stated below.

3.1.1. Pores in the fresh early matured shale

The initial fresh sample is an early matured shale and contains bituminous hydrocarbons formed by kerogen primary cracking (Fig. 1); Organic matter is dominated by algae and exinite with the banded, granular and amorphous shapes (Fig. 1). Fig. 1 shows the petrographic features of this sample. Under blue light excitation, we can observe fluorescent light, lamalginite and sporinite (Fig. 1(a)). Under reflected white light in oil immersion, vitrinite, intertinite and bitumen can be seen in the same area as Fig. 1(b). Fig. 1(c) shows telalginite under blue light excitation and Fig. 1(d) shows sporinite.

Interparticle and intraparticle pores are infilling with the expelled or migrated amorphous bitumen (Fig. 2(a) and (b)). Intercrystalline pores of pyrite framboids are also filled with migrated hydrocarbons (Fig. 2(d)). The artificial shrinkage cracks

can be observed between the organic matter and mineral particles (Fig. 2(c)) and may be caused by the decrease in temperature and confining pressure. However, few organic-matter pores can be detected in Fig. 2(a)–(c).

3.1.2. Pores in the matured shales

Unlike the early matured shales, the complex of organic matter and clays becomes more porous within the matured shales (Fig. 3(a)). Substantial intra-illite pores with organic matter can be observed (Fig. 3(a)). Interparticle pores and shrinkage cracks can be detected at the edge of nonporous lamalginite between organic matter and minerals (Fig. 3(b)). The interparticle pores (Fig. 3(b)) and intercrystalline pores of pyrite can be observed in Fig. 3(c), which are still infilling with migrated oil. Fig. 3(d) shows the concurrent of porous and nonporous organic matter in the matured shale with $%R_0 = 1.06$. Curtis et al. (2012) presented the similar phenomenon in a Woodford shale with $%R_0 = 1.40$ and proposed that the porous organic matter may be gas-prone organic macerals; the nonporous organic matter may be oil-prone organic macerals (Curtis et al., 2012). The intraparticle pores within the carbonate particles and modified mineral pores can also be detected (Fig. 3(e)). However, the irregular morphology of organic-matter pores indicates that the aggregates should be the complex of organic matter with clays, since the migrated hydrocarbon usually present in the modified mineral pores (Fig. 3(e)) and forms bubbly organic-matter pores (Fig. 3(f)) (Loucks and Reed, 2014; Ko et al., 2016). The catalytic effects of clays are supposed to be responsible for this as stated below.

3.1.3. Pores in the high matured shales

Substantial interparticle pores and organic-matter pores occur in the high matured shale with $%R_0 = 1.76$ (Fig. 4). However, interparticle pores are sparse in the unheated shale sample due to strong mechanical compaction (Fig. 2). The significant occurrence

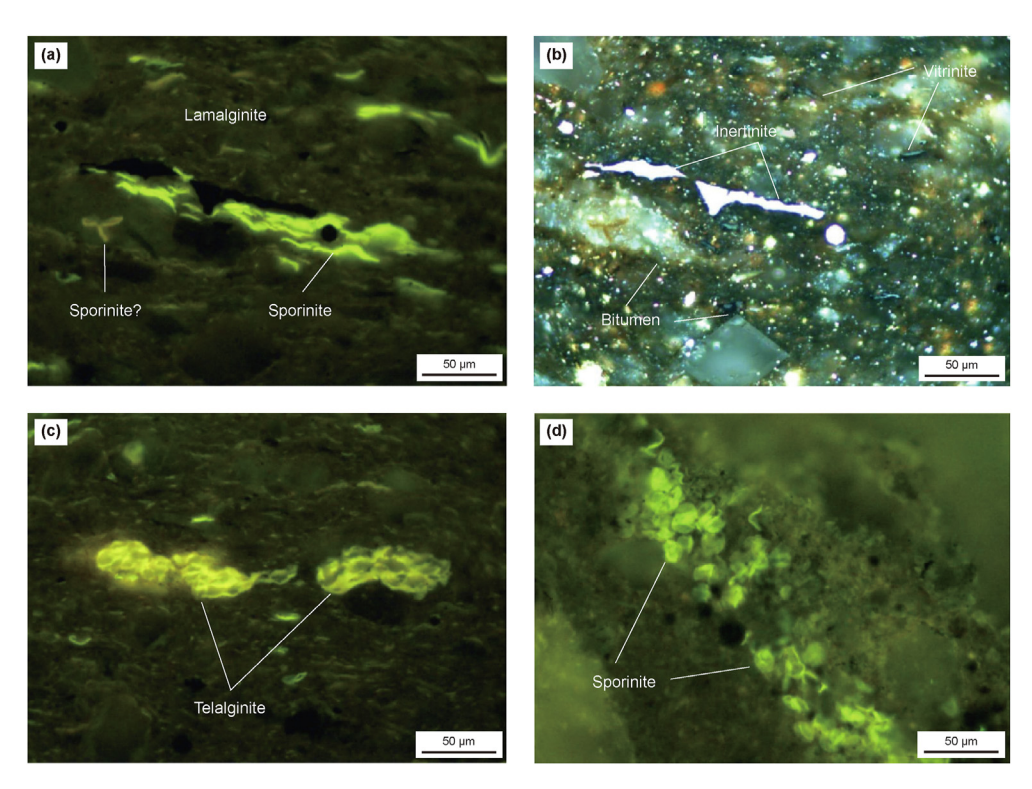


Fig. 1. Photomicrographs showing petrographic features of the fresh unheated shale sample collected from the Upper Cretaceous Nenjiang Formation in the Changling Depression of the Songliao Basin.

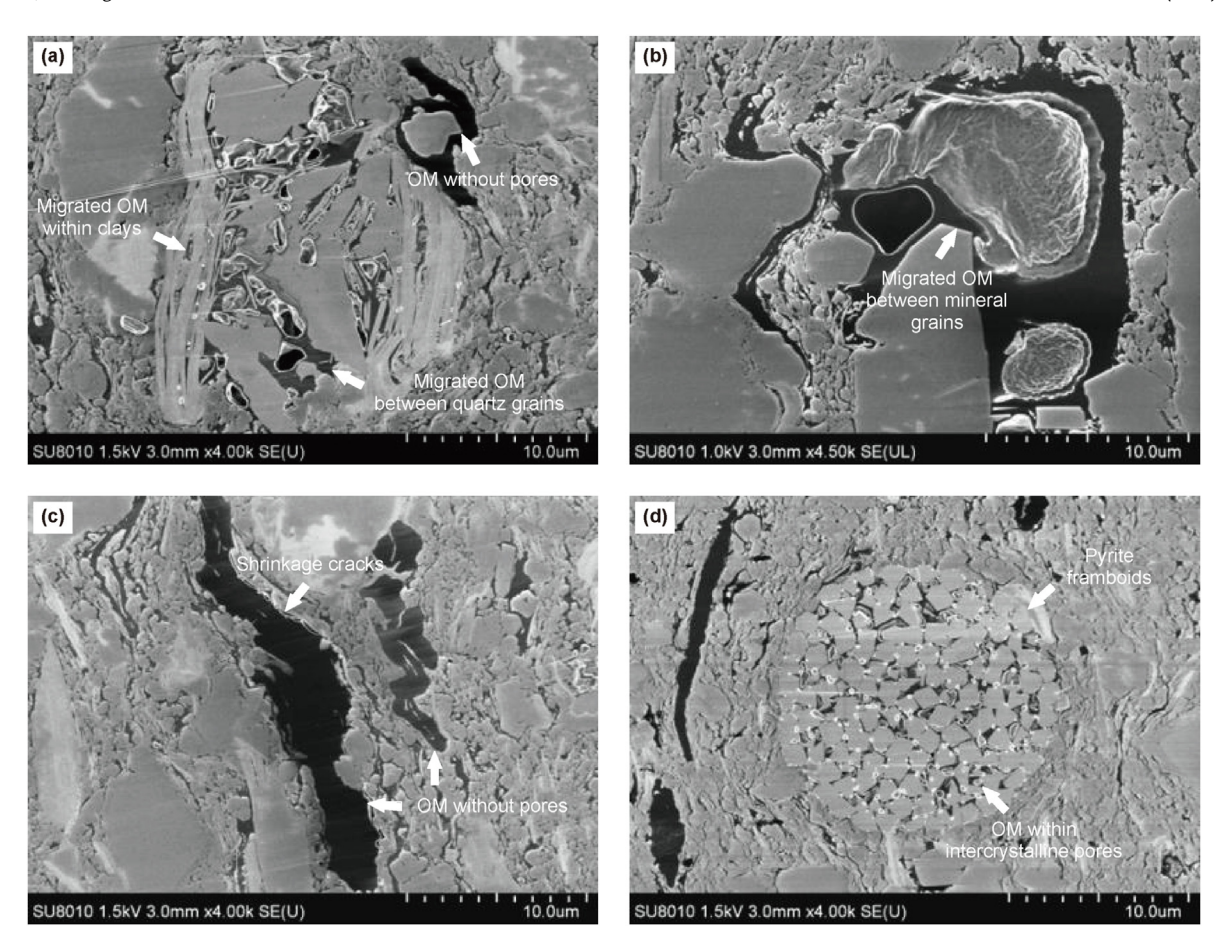


Fig. 2. FE-SEM images acquired in secondary electron model showing nanopores in the unheated natural shale sample ($\Re R_0 = 0.61$) from the Upper Cretaceous Nenjiang Formation in the Changling Depression of the Songliao Basin. **(a)** Mineral matrix pores; **(b)** Interparticle pores; **(c)** Organic matter and minerals; **(d)** Pyrite framboids. OM = organic matter.

of interparticle pores (Fig. 4(a) and (d)) may be caused by thermal decomposition of oil-prone macerals (e.g. algae and exinite) and then hydrocarbon migration out of the source, vacuuming the accommodation of parent kerogen. Fig. 4(b) shows that the configuration of pyrite crystals becomes less sharp than before due to pyrite decomposition (Fig. 2(d) and 3(c)).

The organic matter particle is nonporous (Fig. 4(c)). On the contrary, the spongy organic-matter pores are observed within the complex of organic matter and illite (Fig. 4(d) and (e)). The outer part contacted with minerals are less porous than the central part, indicating at least two phases of illitization.

3.1.4. Pores in the over matured shales

Abundant mineral matrix pores and organic-matter pores can also be detected in the overmatured shales (Fig. 5). More interestingly, the complex of organic matter and illite comprise of two parts (Fig. 5(a)–(c)). The inner part is more porous than the outer (Fig. 5(a)–(c)), indicating at least two phases of illitization. The nonporous pyrobitumen particles with spherical and ellipsoidal shapes are hosted within the microfractures (Fig. 5(d)). The pyrobitumen is assumed to be formed by migrated oil secondary cracking. The supporting evidences refer to the nonporous pyrobitumen within the intercrystalline pores of pyrite framboids (Fig. 5(e) and (f)). The intercrystalline pores of pyrite framboids were infilling by migrated hydrocarbons (Fig. 2(d) and 3(c)). The complete pyrite decomposition results in the formation of artificial organic-matter pores (Fig. 5(e)). In fact, the pyrobitumen particles are nonporous (Fig. 5(f)).

3.2. Pores in the oil cracking experiments with and without illite

Artificial experiments of oil cracking with and without illite were conducted on a crude oil from the Songliao Basin. These experiments were conducted at 400 °C for 72 h with Easy $\Re R_0 = 1.75$. Significant differences can be observed on the morphology of pyrobitumen and associated nanopores in experiments with and without illite (Fig. 6). In the experiment with oil alone, the morphology of pyrobitumen is nearly spherical or elliptical with a few pores in solid pyrobitumen (Fig. 6(a)). Pores can be observed between the solid pyrobitumen particles (Fig. 6(b)). The pyrobitumen in experiment with oil and illite is rod and strip shaped (Fig. 6(c)). Except for pores between the particles of solid pyrobitumen (Fig. 6(c)), the interconnected pores can be observed in the middle of these pyrobitumen (Fig. 6(d)).

3.3. Pore size distribution

According to the classification standards established by the International Union of Pure and Applied Chemistry (IUPAC) (Sing, 1985), pores in the fresh sample are dominated by micropore (<2 nm) and 10–50 nm mesopore (Fig. 7(a) and (b) and Fig. 8(a)). Compared with the untreated initial shale sample, nanopores with different size generally increase with thermal maturity increasing (Fig. 7(a)–(c) and Fig. 8(b) and (c)). 2–10 nm mesopores and macropores present a significant increase at $%R_0 \ge 1.36$ (Fig. 8(d)–(i)).

After solvent extraction by using Soxhlet extractor, the obvious increase in micropores and 2–5 nm mesopores can be detected in

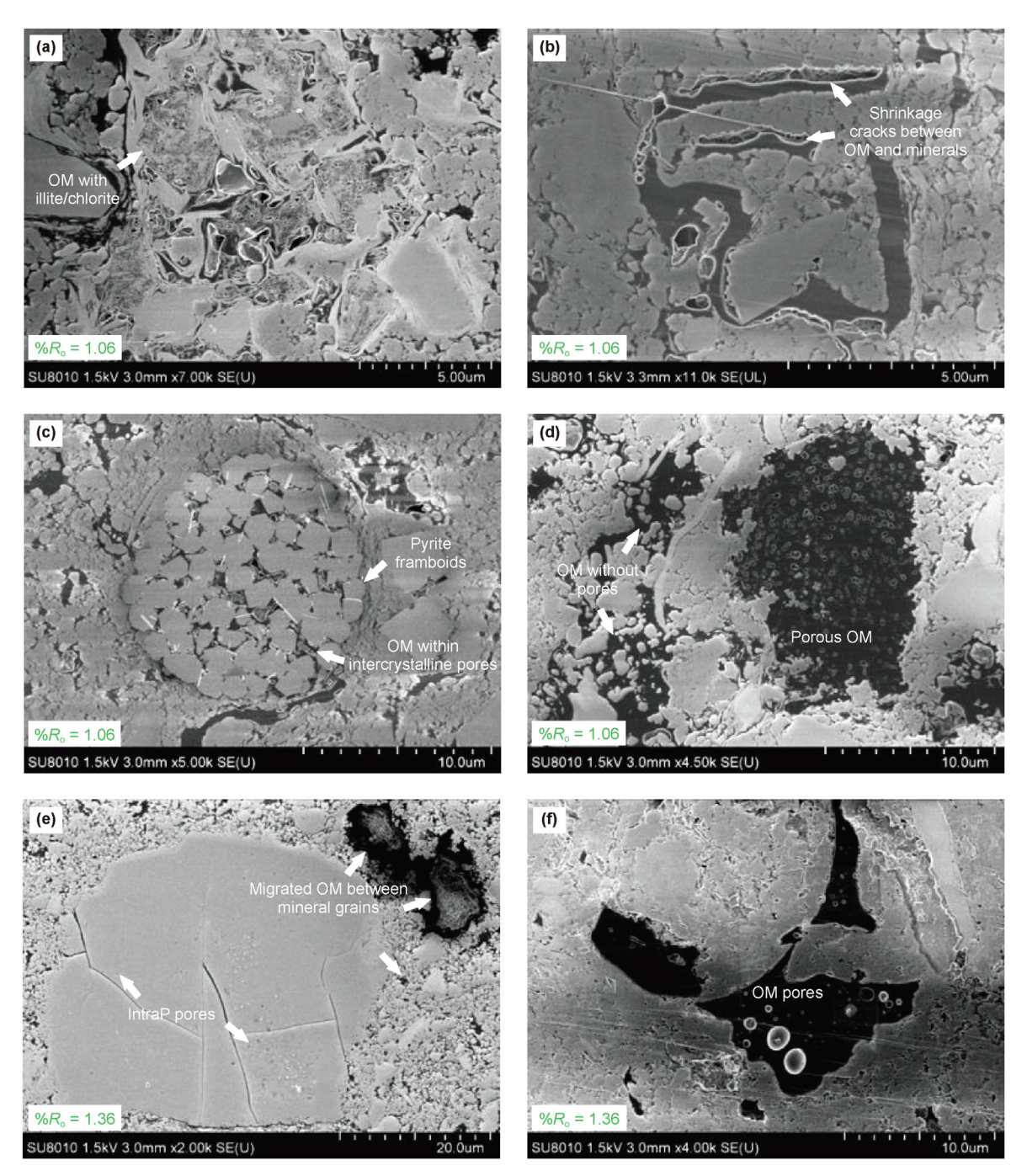


Fig. 3. FE-SEM images acquired in secondary electron model, showing nanopores within the pyrolyzed shale samples in the oil window with $R_0 = 1.06$ (350 °C for 16 h) and 1.36 (400 °C for 12 h). OM = organic matter; intraP = intraparticle.

the fresh shale sample (Fig. 7(c) and (d) and Fig. 8(a)). Compared with the untreated shale sample, the treated samples are significantly enriched in <20 nm pores in the oil window ($\%R_0 = 0.5-1.3$), <10 nm pores in the wet gas window ($\%R_0 = 1.3-2.0$), and <5 nm pores in the early of dry gas window ($\%R_0 = 2.0-3.0$), and present no obvious difference in the late of gas window ($\%R_0 = 3.0-4.0$) (Fig. 8(b)–(i)).

3.4. BJH pore volume

For the untreated shale samples, the total BJH pore volume is $0.004~{\rm cm}^3/{\rm g}$ for the original sample, increases continuously to

0.059 cm³/g at % R_0 = 2.09, decreases slightly to 0.053 cm³/g at % R_0 = 2.47, and then increases slightly to 0.065 cm³/g at % R_0 = 3.00–4.01 (Fig. 9(a)). The micropore volume presents a peak value of 0.004 cm³/g at % R_0 = 1.76, decreases to 0.001 cm³/g at % R_0 = 2.47 and increases continuously to 0.005 cm³/g at % R_0 = 4.01 (Fig. 9(b)). The mesopore volume presents a nearly linear increase from 0.002 to 0.037 cm³/g at % R_0 = 0.61–2.47, and slightly decreases to 0.027 cm³/g at % R_0 = 4.01 (Fig. 9(c)). The macropore volume increases continuously to the peak value of 0.025 cm³/g at % R_0 = 2.09, decreases to 0.016 cm³/g at % R_0 = 2.47 and then shows an increase to 0.034 cm³/g at % R_0 = 4.01 (Fig. 9(d)).

Compared with the untreated shale samples, the total BJH pore

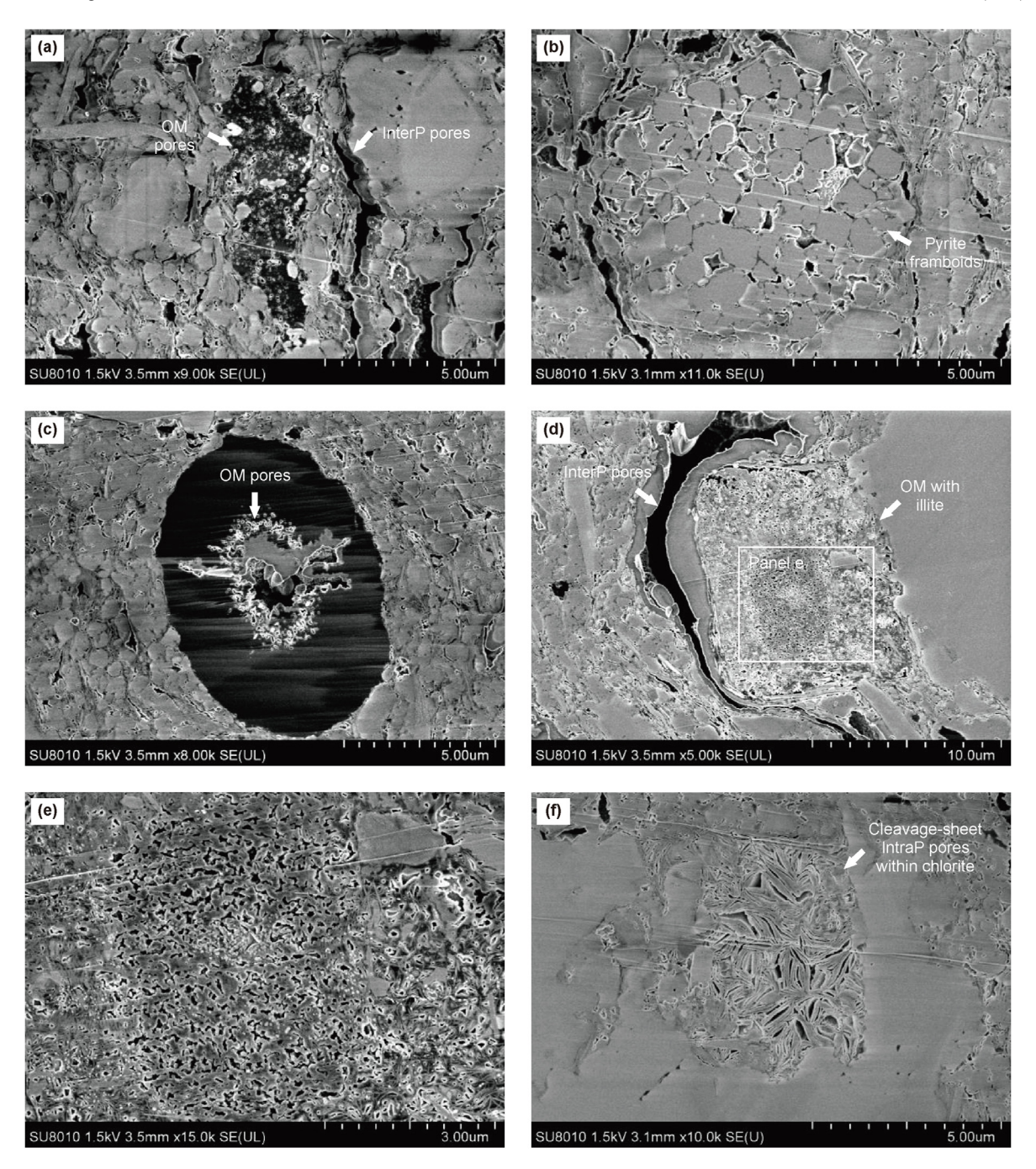


Fig. 4. FE-SEM images acquired in secondary electron model, showing mineral matrix pores and organic-matter pores within the high matured shale samples in the wet gas window with $R_0 = 1.76$ (400 °C for 25 h). OM = organic matter; InterP = interparticle; IntraP = intraparticle.

volume of the treated samples is generally greater in oil and wet gas window and is similar in dry gas window. It presents a consistent increase from $0.007 \, \mathrm{cm^3/g}$ at $\%R_0 = 0.61$ to the peak value of $0.071 \, \mathrm{cm^3/g}$ at $\%R_0 = 1.76$, a slight decrease to $0.056 \, \mathrm{cm^3/g}$ at $\%R_0 = 2.09 - 2.47$ and then increases continuously to $0.066 \, \mathrm{cm^3/g}$ at $\%R_0 = 3.00 - 4.01$ (Fig. 9(a)). The micropore volume for the treated shale samples shows the similar change trend with that for the untreated samples but with greater volumes (Fig. 9(b)). The mesopore volume is generally greater than that for the untreated samples in oil window, increases continuously at $\%R_0 = 0.61 - 1.76$ and approaches the peak value of $0.045 \, \mathrm{cm^3/g}$ at $\%R_0 = 1.76$ and close to that for the untreated samples in dry gas window (Fig. 9(c)).

The macropore volume for the treated samples is greater in oil and wet gas window than that for the untreated samples and is close to that for the untreated samples in dry gas window. It approaches the peak value of 0.034 cm 3 /g at $%R_o = 4.01$ (Fig. 9(d)).

3.5. LECO TOC-S and Rock-Eval

With increasing thermal maturity, TOC for the untreated shales firstly present a slight decrease from 8.16% to 8.02% at $\%R_0=0.61-1.06$, a fast decrease to 4.42% at $\%R_0=1.36$, then a gentle decrease to 3.71% at $\%R_0=1.88$ and finally a slight decrease to 3.12% at $\%R_0=4.01$ (Fig. 10 and Table 1). The relevant TOC for solvent-

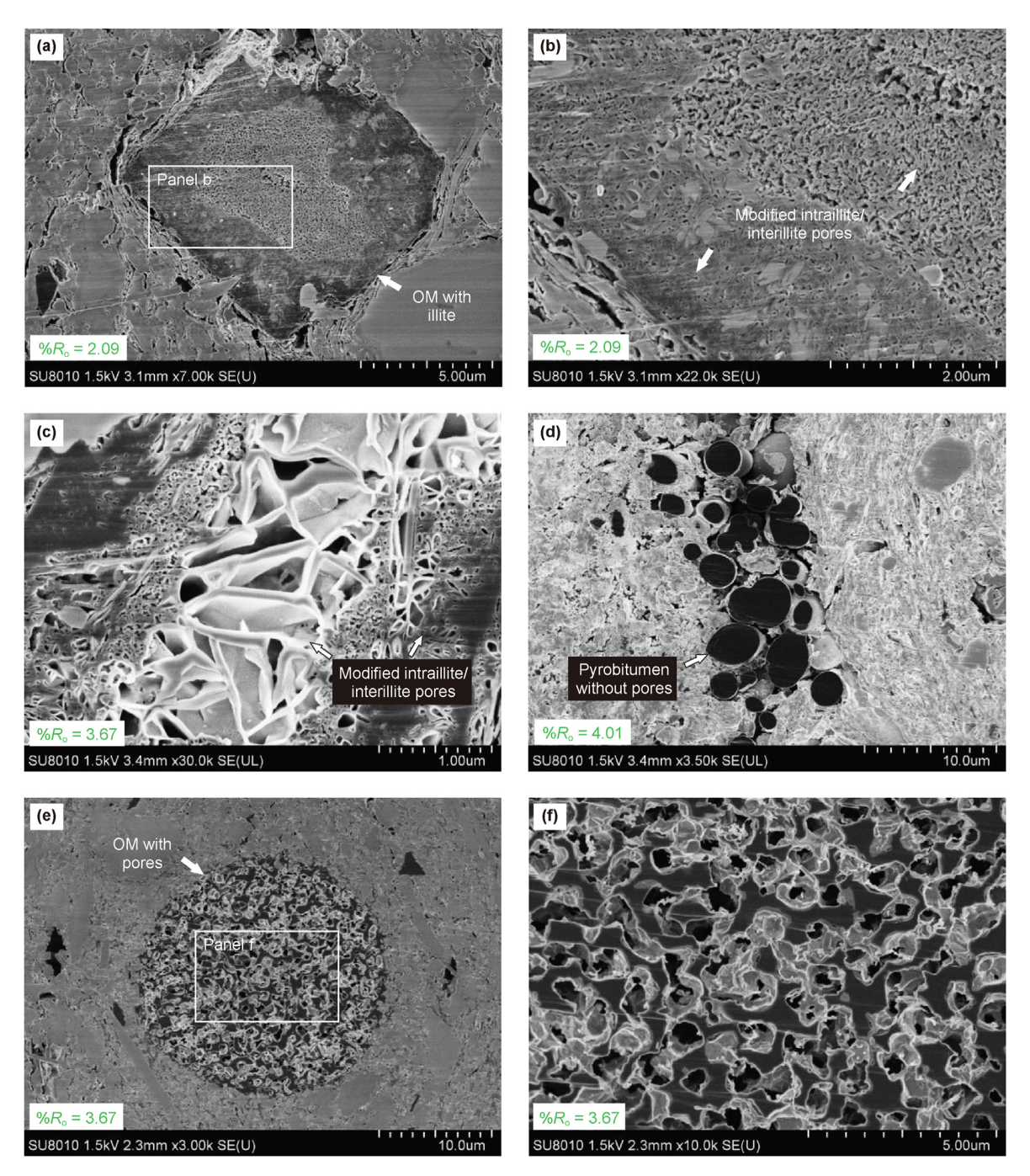


Fig. 5. FE-SEM images acquired in secondary electron model for heated samples in the dry gas window with $%R_0 = 2.09 (450 \, ^{\circ}\text{C})$ for 24 h), 3.67 (550 $\, ^{\circ}\text{C}$ for 24 h) and 4.01 (600 $\, ^{\circ}\text{C}$ for 24 h). (f) The magnified areas marked with white rectangle in (e).

extracted shale samples were generally smaller than that for the untreated samples by showing a quick decrease at $\Re R_0 = 0.67-1.36$, then a continuous increase at $\Re R_0 = 1.36-1.88$, and finally a slight variation (Fig. 10 and Table 1). Significant difference in TOC between the untreated and treated shales was detected at $\Re R_0 = 1.06-1.36$ (Fig. 10 and Table 1).

Unlike TOC, only small difference was detected in S for samples with and without Soxhlet extraction at $\%R_0 = 0.67 - 1.06$ (Fig. 10 and Table 1). Total S decreases gradually with thermal maturity increasing (Fig. 10 and Table 1). Inorganic C is initially 0.35% and then decreases continuously to 0.06% at the end of the experiment.

The S_1 of Rock-Eval pyrolysis for the untreated shale samples

increases significantly from 4.15 to 8.59 mg/g in oil window ($R_0 = 0.61-1.36$), decreases quickly to 2.68 mg/g in wet gas window and presents a slight decrease to 0.08 mg/g in dry gas window. The S_2 of Rock-Eval pyrolysis for the untreated shale samples shows the opposite in oil window by presenting a fast decrease from 60.84 mg/g to 9.29 mg/g at $R_0 = 0.61-1.36$ and decreases slightly in gas window. HI presents the similar change trend as S_2 (Table 1).

3.6. Mineral compositions determined by XRD

Quartz keeps nearly constant at $\%R_0=0.61-1.88$ and shows a general decrease to 51% at the end of the experiments. Illite shows

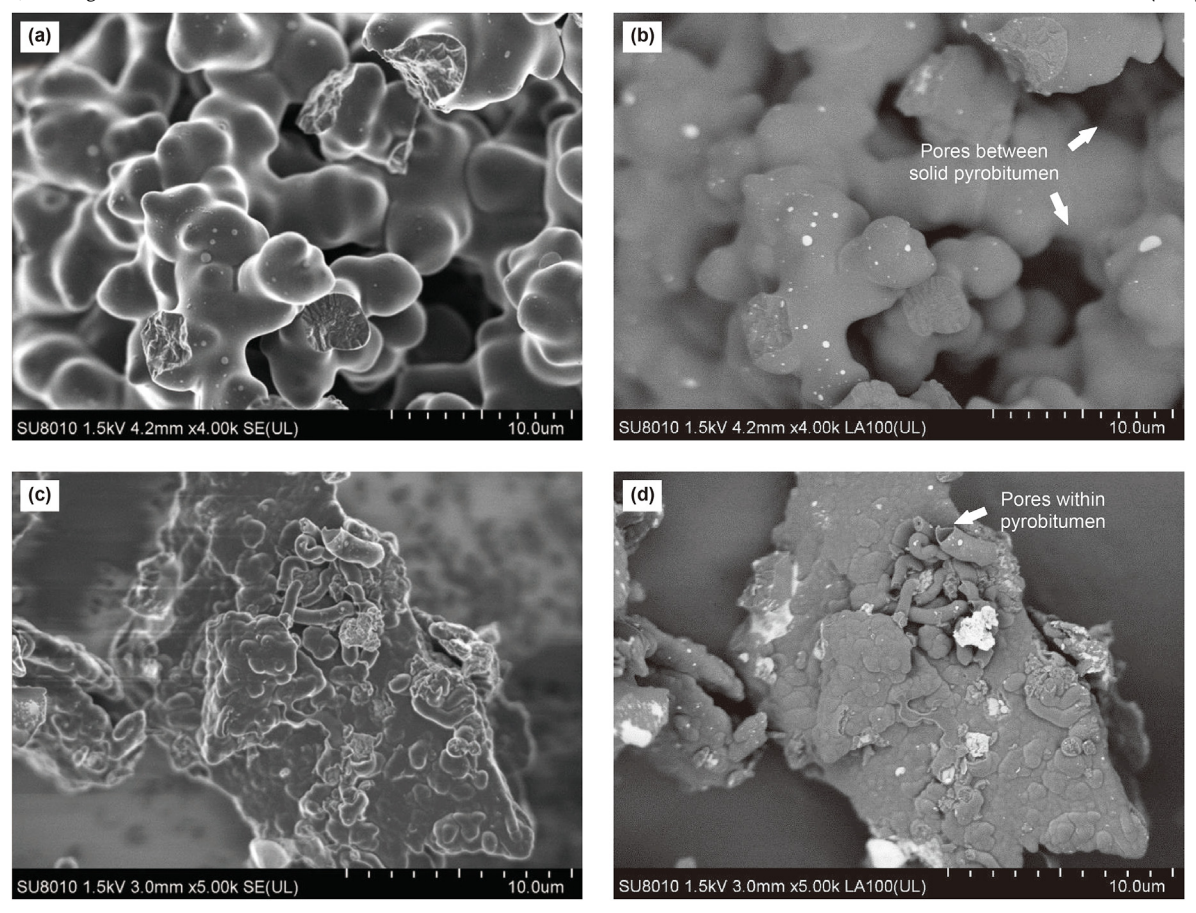


Fig. 6. FE-SEM images acquired in (left) secondary electron (SE) and (right) back scattered electron (BSE) modes showing the nonporous pyrobitumen in experiment with oil alone in (a) and (b), and porous pyrobitumen in experiment with oil and illite in (c) and (d).

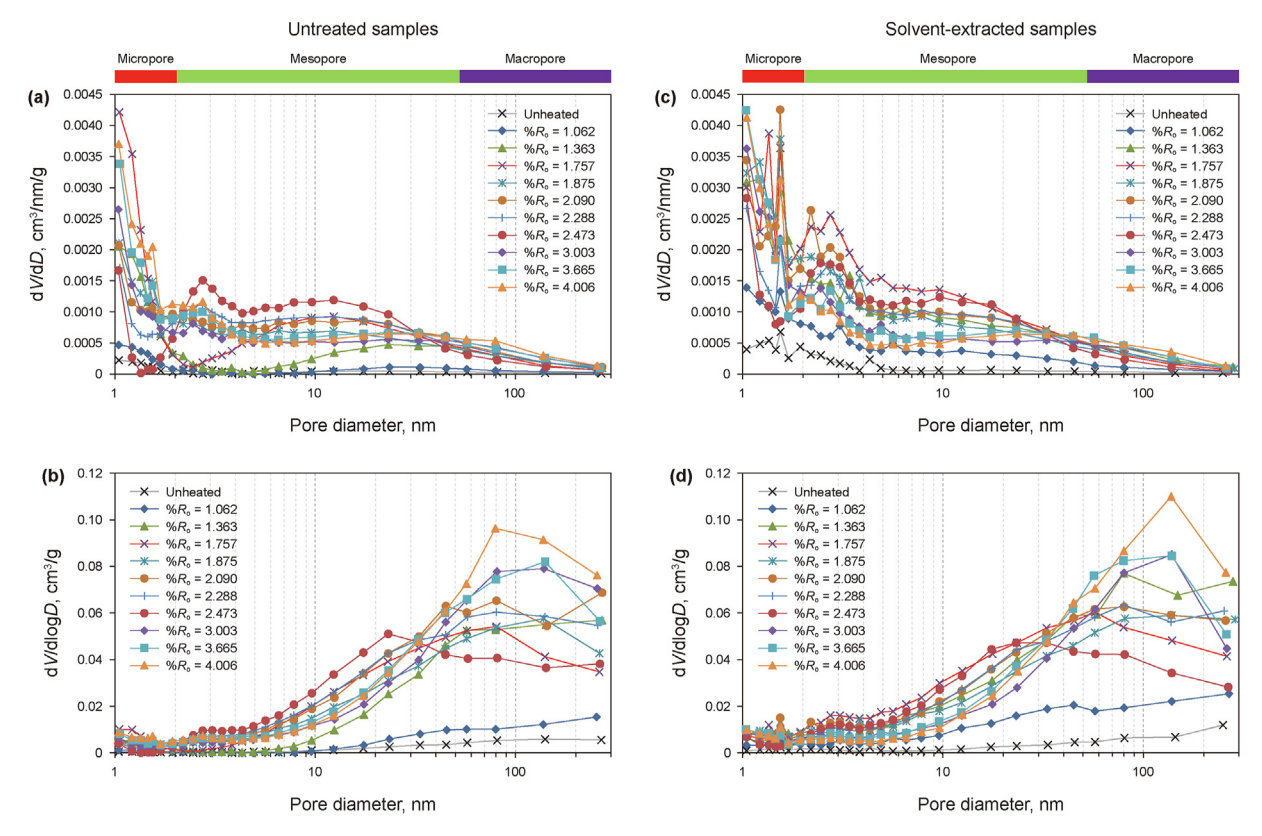


Fig. 7. The plots showing pore size distribution and dV/dD within the natural and heated samples with and without Soxhlet extraction through the experiments. The pore size is derived from the N_2 adsorption using BJH model (Barrett et al., 1951).

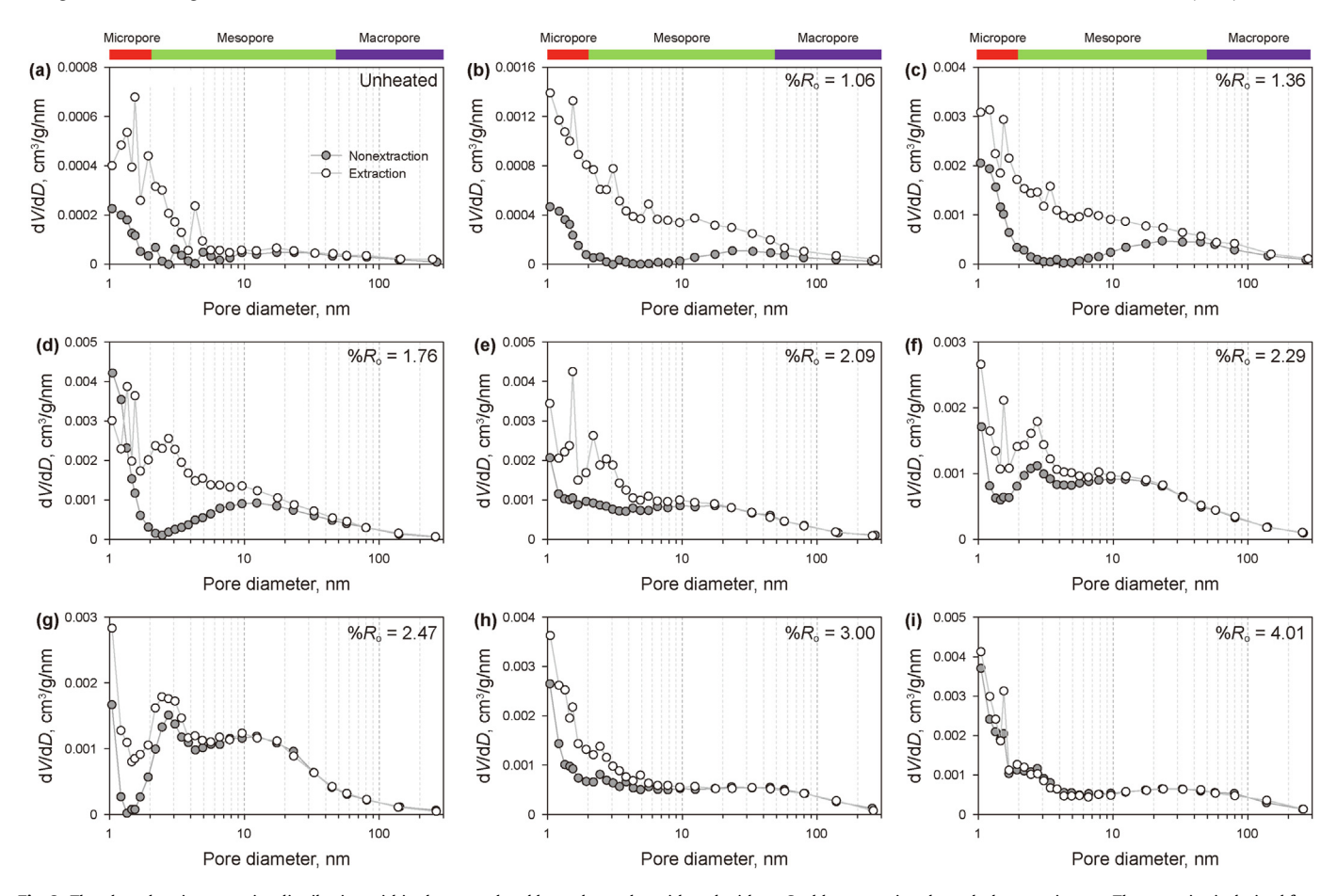


Fig. 8. The plots showing pore size distribution within the natural and heated samples with and without Soxhlet extraction through the experiments. The pore size is derived from the N_2 adsorption using BJH model (Barrett et al., 1951).

the variations with two stages, the first slow increase stage extends from $\Re R_o = 0.67$ to 2.47 and the second fast increase stage ranges from $\Re R_o = 2.47$ to 4.01. The mixed I/S layer presents the opposite trend with illite. No clear change trend can be observed on chlorite and feldspar through the experiments (Fig. 11 and Table 1).

4. Discussion

4.1. Effect of organic matter transformation on the occurrence of nanoporosity

Due to hydrocarbon generation and expulsion out of source rock, the generative organic C will be loss depending on the amount of hydrogen in the original kerogen (Tissot and Welte, 1984). This results in the TOC and HI decrease and transformation ratio increase with increasing thermal maturity (Tissot and Welte, 1984). The various BJH pore volumes present good negative correlations with TOC and positive correlations with TR-HI (Table 2 and Fig. 12), indicating the crucial role of hydrocarbon generation and expulsion in forming nanoporosity within this organic-rich shale. However, liquid oil generation and expulsion, oil secondary cracking into wet gas and pyrobitumen, and dry gas generation may act as distinct roles in the formation of nanopores at the different thermal maturity stages.

4.1.1. Liquid oil generation and expulsion in oil window

Under the experimental conditions, the oil window extends from the early mature to late mature stage ($\%R_0 = 0.61-1.36$). At the

early mature stage ($%R_0 = 0.61$) slight difference of TOC between the untreated and solvent-extracted samples indicates the absence of significant oil generation (Fig. 10). Thus, most mineral-associated pores are partly infilling by the generated hydrocarbons (Fig. 2(a), (b) and (d)), and the BJH pore volume increases slightly from $0.004 \, \mathrm{cm}^3/\mathrm{g}$ for untreated sample to $0.007 \, \mathrm{cm}^3/\mathrm{g}$ for treated sample (Table 1). Compared with sample without Soxhlet extraction, the obvious increase of 1–5 nm pores in sample with Soxhlet extraction indicates that the generated hydrocarbons are hosted mainly within these pores (Fig. 8(a)).

Intensive oil generation without significant expulsion can be observed at $%R_0 = 1.06$. TOC for the untreated sample shows no obvious decrease than that for the fresh sample (Fig. 10). However, after treated with organic solvent, TOC decreases significantly from 8.02% to 5.89% (Table 1 and Fig. 10). The BJH pore volume increases obviously from 0.009 to 0.025 cm³/g (Table 1 and Fig. 9(a)). The porous complex of organic matter and clays and modified mineral pores can be detected (Fig. 3(a)—(d)). Solvent extraction releases a large amount of <50 nm pores (Fig. 8(b)), indicating the generated oil can be expelled out of sources and then migrate into these pores (Fig. 3(a)—(d)).

Significant oil generation and expulsion out of the pyrolyzed shales take place at the late mature stage. This is indicated by a substantial decrease of TOC from 8.02% at $R_0 = 1.06-4.42\%$ at $R_0 = 1.36$ for the untreated samples (Fig. 10 and Table 1). The BJH pore volume responses to this by presenting a significant increase from $0.009 \, \mathrm{cm}^3/\mathrm{g}$ at $R_0 = 1.06 \, \mathrm{to} \, 0.040 \, \mathrm{cm}^3/\mathrm{g}$ at $R_0 = 1.36 \, \mathrm{for}$ the untreated samples (Fig. 9(a)). The BJH pore volume for the treated

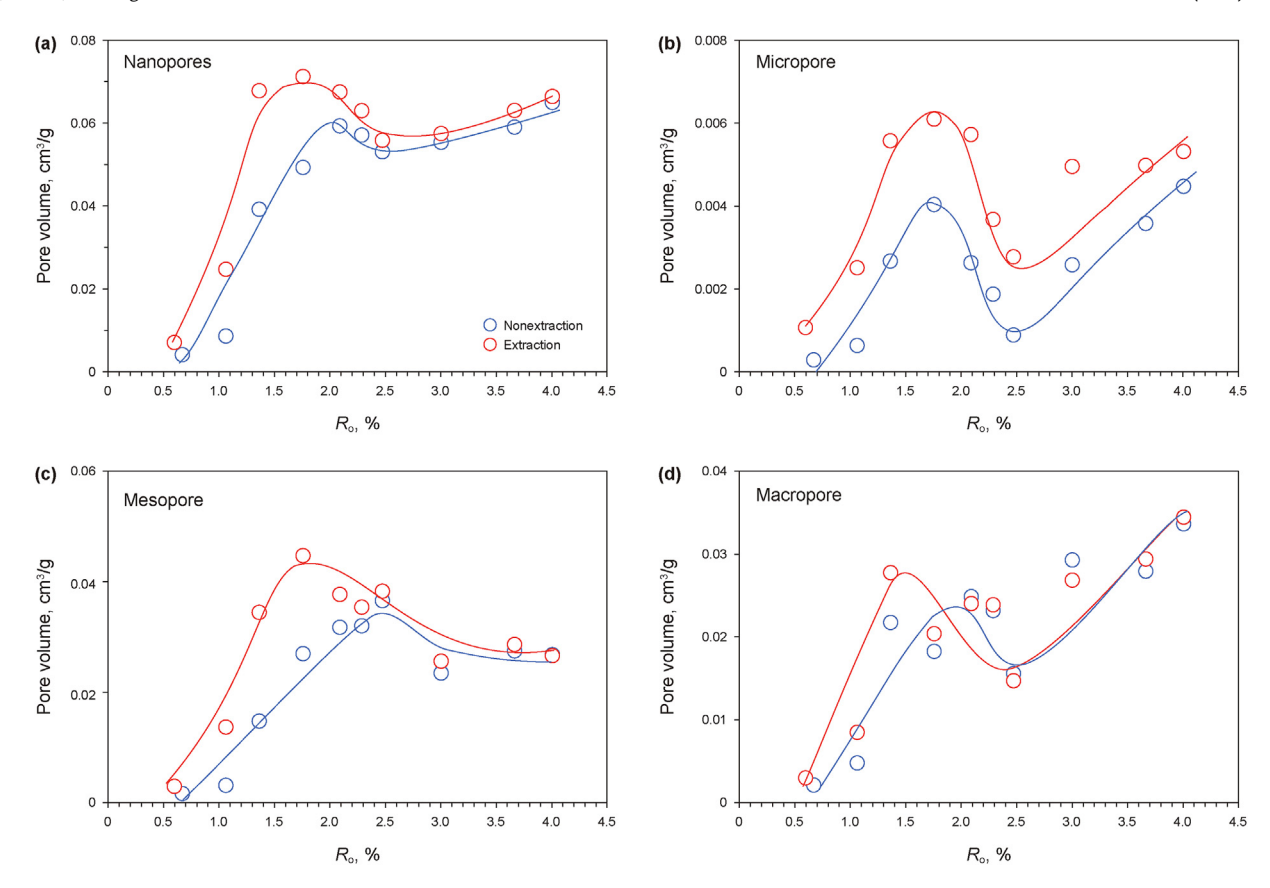


Fig. 9. The plot showing the pore volume (Nanopores, Micropore, Mesopore and Macropore) changing with thermal maturity increasing for the fresh and heated samples through the experiments.

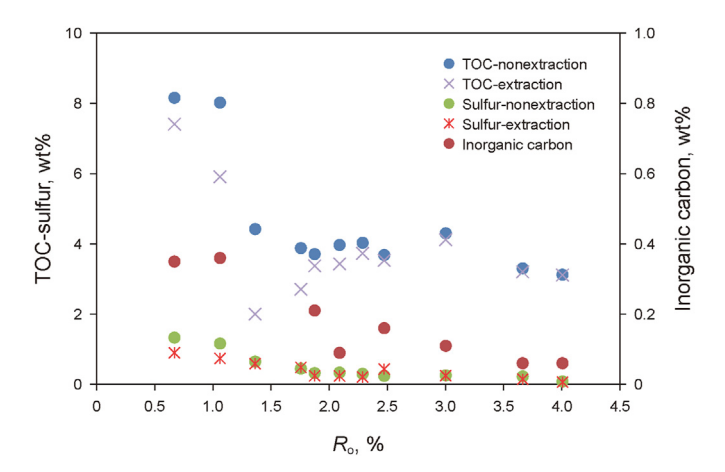
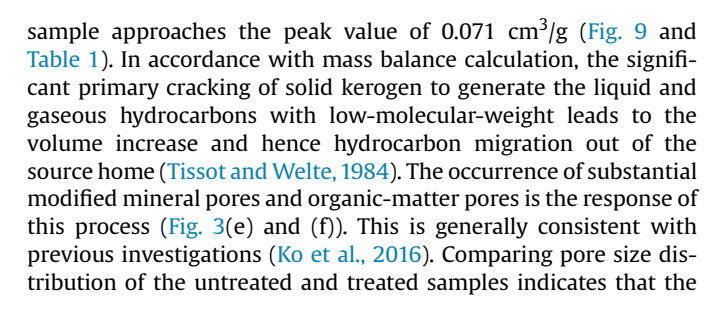


Fig. 10. The plot showing the variations of LECO TOC-S and inorganic C with increasing thermal maturity for the samples with and without Soxhlet extraction.



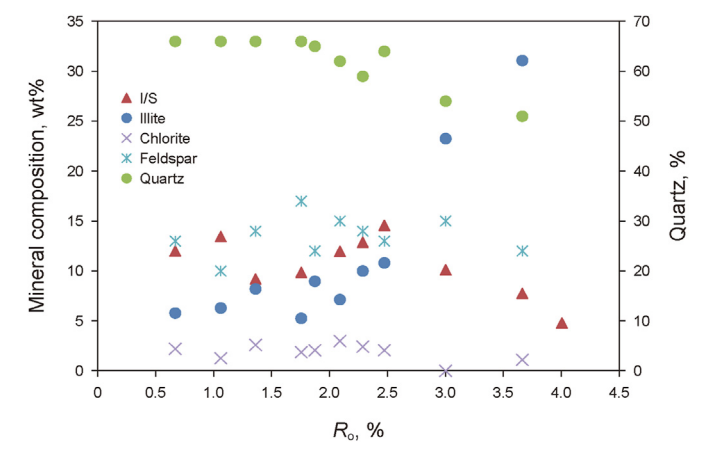


Fig. 11. The plot showing the mineral compositions changing with thermal maturity increasing for the fresh and heated samples through the experiments.

retained crude oil is hosted mainly in <50 nm pores as well as some macropore as shown in Fig. 8(c).

4.1.2. Oil secondary cracking in gas window

It is well known that oil cracking is a disproportionation reaction, and one product is natural gas, the other product is the residual carbon usually referred to as pyrobitumen (Waples, 2000; Hill et al., 2003; Xiong et al., 2016). The onset of oil cracking is considered to be at around $\Re R_0 = 1.0$ (Jarvie et al., 2007), significant oil cracking usually takes place at $\Re R_0 > 1.5-1.6$ (Hill et al., 2003; Xiong et al., 2016). TOC for solvent-extracted samples presents a

Table 2
The correlations between various BJH pore volumes of N_2 adsorption and LECO TOC-S, inorganic C and mineral compositions of fresh and pyrolyzed shale samples with no Soxhlet extraction.

Correlation	$V_{\rm nanopores}$	$V_{ m micropore}$	$V_{ m mesopore}$	V _{macropore}	TOC	Sulfur	C_{iorg}	TR-HI	I/S	Illite	Chlorite	Quartz	Feldspar
V _{Nanopores}	1	1	1			1		1					
$V_{\rm Micropore}$	0.78	1	1	1	1	1	1	1	1	1	1	1	1
$V_{\rm Mesopore}$	0.87	0.56	1	1	1	1	1	1	1	1	1	1	1
$V_{\text{Macropore}}$	0.96	0.81	0.68	1	1	1	1	1	1	1	1	1	/
TOC	-0.95	-0.78	-0.91	-0.86	1	1	1	1	1	1	1	1	1
Sulfur	-0.97	-0.73	-0.92	-0.88	0.97	1	1	1	1	1	1	1	1
C_{iorg}	-0.81	-0.74	-0.73	-0.76	0.82	0.73	1	1	1	1	1	1	/
TR-HI	0.96	0.7	0.94	0.86	-0.97	-0.99	-0.76	1	1	1	1	1	/
I/S	-0.46	-0.78	-0.04	-0.64	0.39	0.35	0.42	-0.27	1	1	1	1	/
Illite	0.56	0.58	0.28	0.66	-0.48	-0.54	-0.27	0.42	-0.77	1	1	1	/
Chlorite	-0.04	-0.22	0.09	-0.11	-0.01	0.07	-0.25	0.01	0.39	-0.64	1	1	1
Quartz	-0.58	-0.47	-0.44	-0.59	0.55	0.61	0.28	-0.51	0.55	-0.94	0.59	1	/
Feldspar	0.18	0.34	0.37	0.03	-0.38	-0.25	-0.46	0.32	0.03	-0.25	0.19	0.08	1

Note: Significant correlation-Correlation coefficient >0.5; $C_{\rm lorg}$ = inorganic carbon; TR-HI = $100-{\rm HI_c/HI_o}\times 100$. Where HI_c is the hydrogen index for the pyrolyzed samples, and HI_o is the hydrogen index for the used original sample; "J''" = No data available.

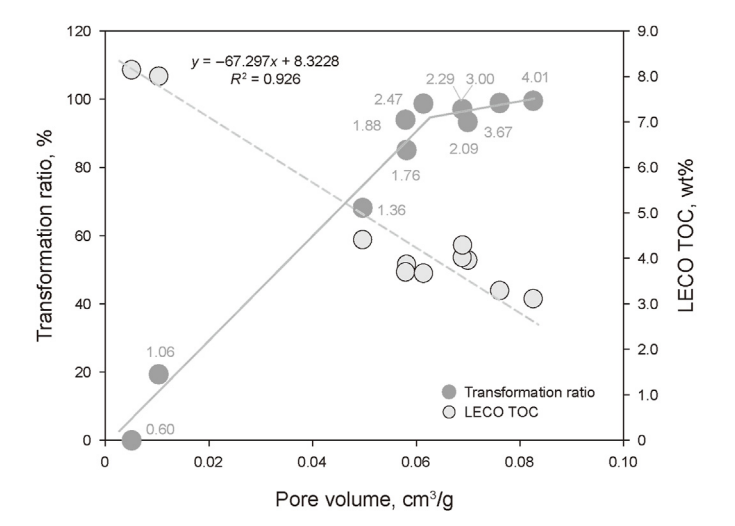


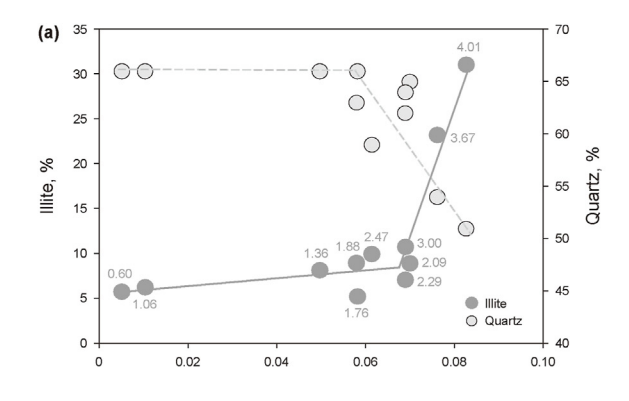
Fig. 12. The crossplots of pore volume versus transformation ratio and TOC for shale samples without Soxhlet extraction, the good correlations indicate the important role of organic matter transformation in nanoporosity formation.

continuous increase at $\Re R_0 = 1.36-2.09$ in wet gas window (Fig. 10). This is supposed to be caused by solid pyrobitumen formation by secondary oil cracking. Moreover, the difference of TOC between the untreated and treated samples becomes gradually smaller (Fig. 10). This also indicates the enhanced oil secondary cracking

and pyrobitumen formation with increasing thermal maturity.

The oil secondary cracking in wet gas window favors the formation of various nanopores. This is indicated by the persistent increase of the BJH pore volume for the untreated samples (Fig. 9(a)). The significant occurrence of interparticle pores and organic-matter pores can be detected within samples in wet gas window (Fig. 4). However, mineral matrix pores, in particular interparticle pores are nonnative, since interparticle pores are scarce in the unheated shale sample due to strong mechanical compaction (Fig. 2). These pores are assumed to be the home of hydrocarbon sources such as algae and exinite (Fig. 1), organic matter transformation and the generated hydrocarbon migrating out of the source home result in the occurrence of abundant interparticle pores and organic-matter pores (Fig. 4).

The effects of pyrobitumen formation have two folds: (1) solid pyrobitumen formation can decrease the total pore volume. Solvent extraction unlocks mainly <20 nm pores for sample at $%R_0 = 1.76$ (Fig. 8(d)) but mainly <10 nm pores for sample at $%R_0 = 2.09$ (Fig. 8(e)). This is due to more pyrobitumen formed by consuming the extractable liquid oil, resulting in a continuous decrease of various pore volumes for the treated samples at $%R_0 = 1.76-2.49$ (Fig. 9 and Table 1). (2) Solid pyrobitumen can host abundant organic-matter pores. As previous studies (Jarvie et al., 2007; Loucks et al., 2012; Wang et al., 2023), substantial organic-matter pores can be detected within the shale samples in wet gas window, in particular the complex of organic matter and clays (Fig. 4). This may have a significant contribution to the pore volume increase for the untreated samples in wet gas window, though



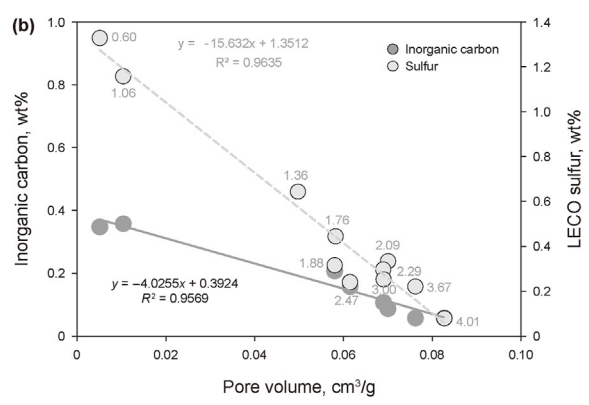


Fig. 13. The crossplots of pore volume versus (a) illite and quartz, and (b) inorganic C and LECO S for shale samples without Soxhlet extraction, the good correlations indicate the important role of mineral transformation in nanoporosity formation.

pyrobitumen in modified minerals is nonporous (Fig. 4).

4.1.3. Dry gas generation in gas window

In dry gas window mineral matrix pores and organic-matter pores can be extensively detected (Fig. 5). No substantial difference can be observed on TOC (Fig. 10), pore diameter distribution (Fig. 8(f)—(i)) and pore volumes (Fig. 9(a) and Table 1) between the untreated and solvent-extracted samples. This indicates little extractable hydrocarbons left within the pyrolyzed shales. C_2 + gaseous compounds can be thermally cracked intensively (Waples, 2000; Hill et al., 2003; Xiong et al., 2016; Xiao et al., 2019). This may favor the formation of micropore within the organic matter particles as suggested by the micropore volume increase at $R_0 = 2.49$ —4.01 (Fig. 9(b)). The increase of macropore volume at this stage as shown in Fig. 9(d) may be caused mainly by mineral transformation as stated below.

4.2. Effect of mineral transformation on the occurrence of nanoporosity

Under the experimental conditions, mineral transformation includes illitization of clay minerals, quartz dissolution, and pyrite and carbonate decomposition. Good correlations between mineral compositions and pore volumes as shown in Table 2 and Fig. 13 indicate that mineral transformation as the result of the organic-inorganic interactions also has an important role in the development of nanoporosity within organic-rich shale samples.

4.2.1. Clay illitization

Clay illitization requires the aluminum and potassium. The occurrence of organic acids during oil generation may promote the K-feldspar dissolution by Eq. (1) (Smith and Ehrenberg, 1989; Hutcheon et al., 1993):

$$KAlSi_3O_8 + 4H^+ = K^+ + Al^{3+} + 3H_4SiO_4$$
 (1)

This provides the required elements and hence favors the illite precipitation by Eq. (2) (Johns and McKallip, 1989) as indicated by good negative covariation between I/S mixed layers and illite (r = -0.77) as shown in Table 2 and Fig. 13(a).

$$K^{+} + Al^{3+} + smectite = illite + Si^{4+}$$
 (2)

In gas window the hydrogen generation by the cyclization and aromatization of organic molecules (Tissot and Welte, 1984) may provide the opportunity for pyrite decomposition by Eqs. (3) and (4) to release the acid gas of hydrogen sulfide (Rickard, 2007). This may result in the chlorite dissolution by Eq. (5) due to the occurrence of sufficient acids (Genuise, 1991).

$$FeS_2 + H_2 = FeS + 2H_2S \tag{3}$$

$$FeS + 2H^{+} = Fe^{2+} + H_2S \tag{4}$$

$$\begin{split} &(Al_{1.77}Fe_{3.27}Mg_{0.96})Si_{2.89}Al_{1.11}O_{10}(OH)_8+17.1H^+=2.88\\ &Al^{3+}+3.27Fe^{2+}+0.96Mg^{2+}+2.89\ H_4SiO_4+6.72H_2O \end{split} \label{eq:continuous} \tag{5}$$

The supply of aluminum, iron, and magnesium may favor the formation of illite by Eq. (6) (Lynch, 1996). This is suggested by the negative correlation between chlorite and illite (Table 2) and results in a fast increase of illite in dry gas window (Fig. 7).

$$\begin{split} 65\text{K}^{+} + 0.08\text{Na}^{+} + 0.14\text{Fe}^{2+} + 0.2\text{Mg}^{2+} + 3.4\text{H}_{4}\text{SiO}_{4} + \\ 2.27\text{Al}^{3+} &= \text{K}_{0.65}\text{Na}_{0.08}(\text{Al}_{1.68}\text{Fe}_{0.14}\text{Mg}_{0.2})(\text{Si}_{3.41}\text{Al}_{1.59}) \\ O_{10}(\text{OH})_{2} + 8.22\text{H}^{+} + 2.69\text{H}_{2}\text{O} \end{split} \tag{6}$$

Illite presents good positive correlations with the volumes of total pore (r = 0.56), micropore (r = 0.58) and macropore (r = 0.66) (Table 2). This indicates that the occurrence of illite is feasible for the development of nanoporosity and is generally consistent with FE-SEM observation (Fig. 3(a) and 4(d)–(e) and 5(a)–(c)). This may be due to two reasons: (I) the complex of illite and organic matters acts as the home of oil-prone kerogens within the fresh shale (Fig. 2). The pyrolyzed shales can host the generated oil due to the strong retention capability of illite (Grim, 1968); (II) the catalytic effects of illite promote volatile hydrocarbons generation during kerogen primary cracking (Tannenbaum et al., 1986) and oil secondary cracking (Zhang et al., 2023; Xiao et al., 2011), and hence favors the formation of organic matter nanoporosity as indicated by the oil cracking experiments with and without illite (Fig. 6). This may be responsible for the early occurrence of organic-matter pores at $%R_0 = 1.06$ in oil window (Fig. 3(d)).

4.2.2. Quartz dissolution

In order to supply enough H_4SiO_4 for the formation illite by Eq. (6), quartz dissolution may take place by Eq. (7) (Milliken, 2003):

$$SiO_2 + H_2O = H_4SiO_4$$
 (7)

Under the experimental conditions the occurrence of quartz dissolution is indicated by the significant decrease in dry gas window (Fig. 7). Quartz dissolution favors the formation of macropores. This is suggested by the good negative correlations between quartz and the volumes of total pore (r=-0.58) and macropore (r=-0.59) (Table 2 and Fig. 10(a)).

4.2.3. Pyrite decomposition

Small difference can be detected in S for samples with and without Soxhlet extraction in oil window (Fig. 10). This indicates that inorganic S-containing minerals such as pyrite are dominated within the shales rather than organic S-containing compounds (Fig. 2). The total S decrease with thermal maturity increasing indicates the decomposition of pyrite by Eqs. (3) and (4). In fact, the significant occurrence of pyrite decomposition was detected at % $R_0 \geq 1.76$ by FE-SEM observation (Fig. 4(b) and 5(e)–(f)). The complete decomposition of pyrite framboids results in forming artificial porous pyrobitumen at % $R_0 = 3.67$ with the pore configuration of pyrite crystal (Fig. 5(e) and (f)). This process is feasible for the formation of various nanopores as indicated by the good negative correlations between S and pore volumes (Table 2 and Fig. 13(b)).

4.2.4. Carbonate decomposition

The acid-generating reaction of illite precipitation by Eq. (6) may lead to the dissolution of carbonates by Eq. (8):

$$CaCO_3 + 2H^+ = Ca^{2+} + CO_2 + H_2O$$
 (8)

The decomposition of carbonate is suggested by the continuous decrease in inorganic C through the experiments (Table 1). The decomposition of carbonate favors the formation of nanopores. This is indicated by the strong negative correlations between inorganic C and pore volumes (Table 2 and Fig. 13(b)). The intraparticle pores can be detected in the calcite particles at $%R_0 = 1.36$ induced by carbonate dissolution (Fig. 3(e)).

5. Geological implications

Formation and evolution of nanoporosity within the organicrich shales during thermal maturation has important implications in evaluating sweet spots for shale-oil and shale-gas plays. Our

experimental results show that the complex of organic matter and clays contains oil-prone kerogen and is prone to generating liquid oil (Figs. 3–5). Strong adsorption capacity of illite is feasible for retaining more oil (Grim, 1968; Tannenbaum et al., 1986; Huizinga et al., 1987; Mayer, 1994). This provides the opportunity for the complex to act as the source at the elevated thermal maturity.

More importantly, pore volume for storing hydrocarbon fluids approaches the maximum at $%R_0 = 1.36$ and presents only a slight decrease to $%R_0 = 1.76$. This coincides with the occurrence of significant hydrocarbon expulsion as suggested by the significant reduction of TOC and increase of TR-HI (Fig. 10 and Table 1). So, the sweet spot may prefer to be located in the wet gas window. Strong mechanical compaction can promote oil expulsion much earlier in the subsurface and hence may extend it to the late mature stage.

In fact, the intraformational oil migration has been identified within the shale oil plays such as Barnett, Bakken and Niobrara shale oil plays in the North American (Han et al., 2015, 2017) and the Qingshankou and Lucaogou shale oil plays in China (Liang et al., 2018; Li et al., 2023). Sweet spots are associated intimately with the organic-lean intervals close to the organic-rich shale beds (Han et al., 2015, 2017; Xin et al., 2022; Mei et al., 2023; Guo et al., 2023). Moreover, the sweet spot of Qingshankou or Gulong shale oil play in the Songliao Basin (China) is actually located mainly in the source kitchen with $\Re R_0 = 1.2-1.7$ (Zhang et al., 2023).

Organic-matter pores act as a crucial role in the storage and productivity for shale gas plays (Jarvie et al., 2007; Loucks et al., 2012; Hao et al., 2013). The main formation pathways of organicmatter pores are considered to be associated closely with oil cracking (Jarvie et al., 2007; Bernard et al., 2012; Curtis et al., 2012; Ko et al., 2016). However, our experimental results show that the pyrobitumen as one of the products of oil cracking is not necessarily porous as suggested by the nonporous pyrobitumen in the intraparticle pores within pyrite framboids (Fig. 4) and microfractures in gas window (Fig. 5), reducing the total pore volumes of shale reservoirs (Figs. 5(d)–(f) and 11(a)–(b)). The absence of catalytic effects of illite formed by the organic-inorganic interactions may be responsible for this. Moreover, carbonate and quartz dissolution induced by illite precipitation have an important contribution to total pore volume increase (Table 2 and Fig. 11). This highlights the important role of mineral matrix pores derived from the organicinorganic interaction in shale-gas reservoirs and has been proved by the recent studies on the Lacustrine Jurassic Da'anzhai shale-gas play in the Central Sichuan Basin (Zhang et al., 2022) and Triassic Chang 7 shale-gas play in Ordos Basin of China (Cui et al., 2019).

6. Conclusions

This study presents the detailed variations of pore types and pore network within an organic-rich mudstone during thermal maturation in a closed pyrolysis system with the presence of water. The following conclusions can be obtained:

- 1. Organic matter transformation has an important impact on the formation and evolution of nanopores. In oil window significant oil generation and migration out of sources results in the occurrence of abundant modified mineral pores with few organic-matter pores, and the maximum pore volume for hydrocarbon storage can be obtained at the late mature stage. In wet gas window intensive hydrocarbon secondary cracking favors the formation of abundant organic-matter pores and mineral matrix pores. Solid pyrobitumen formation can reduce the pore volume. Dry gas generation at the overmature stage is feasible for forming numerous organic-matter micropores.
- 2. The occurrence of nanoporosity within organic-rich shales is affected by the organic-inorganic interactions. The organic-

inorganic interactions may promote clay illitization and hence facilitate the retained oil secondary cracking to form organic-matter pores due to the catalytic effects of illite. Pyrobitumen in modified mineral matrix pores and microfractures are relatively much less porous due to the absence of illite catalyzation. The pyrite decomposition and quartz and carbonate dissolution tend to form various pores.

3. This study reconstructs the whole map of the formation and evolution of pore types and pore network in organic-rich shale and reveals the underlying controls for the occurrence of pores in oil and gas window. This improves our understanding of shale-oil and shale-gas reservoir formation and enrichment, and should be helpful in evaluating sweet spots for shale-oil and shale-gas plays in sedimentary basins.

CRediT authorship contribution statement

Yong Tang: Writing — original draft, Resources, Methodology, Investigation, Conceptualization. Chu-Xiong Li: Visualization, Validation, Investigation, Formal analysis, Conceptualization. Hong Cheng: Resources, Investigation, Formal analysis, Conceptualization. Su-Yang Cai: Validation, Investigation, Data curation. Xiao Li: Writing — review & editing, Investigation, Formal analysis. Qi-Lin Xiao: Writing — review & editing, Visualization, Validation, Supervision, Methodology, Formal analysis, Data curation. Meng-Lin Zheng: Resources, Methodology, Formal analysis. Jin Pan: Visualization, Validation, Methodology, Investigation, Conceptualization.

Declaration of competing interest

The authors declare that they have no known competing financial interests or personal relationships that could have appeared to influence the work reported in this paper.

Acknowledgements

We appreciate the grants from National Nature Science Foundation of China (No. 42030803, 42073066), and the valuable comments and suggestions by three anonymous referees that greatly improved this paper.

References

- Barrett, E.P., Joyner, L.G., Halenda, P.P., 1951. The determination of pore volume and area distributions in porous substances. I. Computations from nitrogen isotherms. J. Am. Chem. Soc. 73, 373–380. https://doi.org/10.1021/ja01145a126.
- Bernard, S., Wirth, R., Schreiber, A., Schulz, H.M., Horsfeld, B., 2012. Formation of nanoporous pyrobitumen residues during maturation of the Barnett shale (Fort Worth Basin). Int. J. Coal Geol. 103, 3–11. https://doi.org/10.1016/ i.coal.2012.04.010.
- Chen, J., Xiao, X., 2014. Evolution of nanoporosity in organic-rich shales during thermal maturation. Fuel 129, 173–181. https://doi.org/10.1016/i.fuel.2014.03.058.
- Chen, Z., Wang, T., Liu, Q., Zhang, S., Zhang, L., 2015. Quantitative evaluation of potential organic-matter porosity and hydrocarbon generation and expulsion from mudstone in continental lake basins: a case study of Dongying sag, eastern China. Mar. Petrol. Geol. 66, 906–924. https://doi.org/10.1016/ i.marnetgeo.2015.07.027.
- Cui, J.W., Zhu, R.K., Luo, Z., Li, S., 2019. Sedimentary and geochemical characteristics of the triassic Chang 7 member shale in the southeastern Ordos Basin, Central China. Pet. Sci. 16, 285–297. https://doi.org/10.1007/s12182-019-0307-9.
- Curtis, M.E., Cardott, B.J., Sondergeld, C.H., Rai, C.S., 2012. Development of organic porosity in the Woodford Shale with increasing thermal maturity. Int. J. Coal Geol. 103, 26—31. https://doi.org/10.1016/j.coal.2012.08.004.
- Fabio, L.B., Marcelle, M.E., Sandra, N.T., Rubson, P.M., Francisco, H.B., Fabrizio, B., Valéria, C.C., Flávia, G.S., José, A.B., Celso, P.F., João, P.T.F., 2022. Karstified layers and caves formed by superposed epigenic dissolution along subaerial unconformities in carbonate rocks impact on reservoir-scale permeability. Mar. Petrol. Geol. 138, 105523. https://doi.org/10.1016/j.marpetgeo.2022.105523.
- Genuise, J.J., 1991. Petrography and Geochemistry of Authigenic Chlorite from

Cretaceous and Oligocene Sandstones of the Texas. Louisiana Gulf Coast University of Texas at Austin (unpublished).

- Grim, R.E., 1968. Clay Mineralogy, second ed. McGraw Hill Book Co., Inc., New York. Guo, H.J., Jia, W.L., Peng, P.A., Ru, L., 2017. Evolution of organic matter and nanometer-scale pores in an artificially matured shale undergoing two distinct types of pyrolysis: a study of the Yanchang Shale with Type II kerogen. Org. Geochem. 105, 56–66. https://doi.org/10.1016/j.orggeochem.2017.01.004.
- Guo, Q.H., Li, S.X., Jin, Z.K., Zhou, X.P., Liu, C.L., 2023. Characteristics and exploration targets of Chang 7 shale oil in triassic yanchang formation, Ordos Basin, NW China. Petrol. Explor. Dev. 50, 878–893. https://doi.org/10.1016/S1876-3804(23) 60435-5
- Han, Y.J., Mahlstedt, N., Horsfield, B., 2015. The Barnett Shale: compositional fractionation associated with intraformational petroleum migration, retention, and expulsion. AAPG Bull. 99, 2173—2202. https://doi.org/10.1306/06231514113.
- Han, Y.J., Horsfield, B., Wirth, R., Mahlstedt, N., Bernard, S., 2017. Oil retention and porosity evolution in organic-rich shales. AAPG Bull. 101, 807–827. https:// doi.org/10.1306/09221616069.
- Hao, F., Zou, H.Y., Lu, Y.C., 2013. Mechanisms of shale gas storage: implications for shale gas exploration in China. AAPG Bull. 97, 1325–1346. https://doi.org/ 10.1306/02141312091.
- He, M., Wang, Z.Y., Moldowan, M.J., Peters, K., 2022. Insights into catalytic effects of clay minerals on hydrocarbon composition of generated liquid products during oil cracking from laboratory pyrolysis experiments. Org. Geochem. 163, 104331. https://doi.org/10.1016/j.orggeochem.2021.104331.
- Hill, R.J., Tang, Y.C., Kaplan, I.R., 2003. Insights into oil cracking based on laboratory experiments. Org. Geochem. 34, 1651–1672. https://doi.org/10.1016/S0146-6380(03)00173-6.
- Hou, Y., He, S., Wang, J., Harris, N.B., Cheng, C., Li, Y., 2015. Preliminary study on the pore characterization of lacustrine shale reservoirs using low pressure nitrogen adsorption and field emission scanning electron microscopy methods: a case study of the Upper Jurassic Emuerhe Formation, Mohe basin, northeastern China. Can. J. Earth Sci. 62, 294–306. https://doi.org/10.1139/cjes-2014-0188.
- Huizinga, B.J., Tannenbaum, E., Kaplan, I.R., 1987. The role of minerals in thermal alteration of organic matter-Ill: generation of bitumen in laboratory experiments. Org. Geochem. 11, 591–604. https://doi.org/10.1016/0146-6380(87) 90012-X.
- Hutcheon, I., Shevalier, M., Abercrombie, H.J., 1993. pH buffering by metastable mineral-fluid equilibria and evolution of carbon dioxide fugacity during burial diagenesis. Geochem. Cosmochim. Acta 57, 1017–1027. https://doi.org/10.1016/ 0016-7037(93)90037-W.
- Jarvie, D.M., 2012. Shale resource systems for oil and gas: Part 2—Shale-oil resource systems. In: Breyer, J.A. (Ed.), Shale Reservoirs—Giant Resources for the 21st Century, vol. 97. AAPG Mem, pp. 89—119. https://doi.org/10.1306/ 13321447.M973489.
- Jarvie, D.M., Hill, R.J., Ruble, T.E., Pollastro, R.M., 2007. Unconventional shale-gas systems: the Mississippian Barnett Shale of north-central Texas as one model for thermogenic shale-gas assessment. AAPG Bull. 91, 475–499. https://doi.org/ 10.1306/12190606068.
- Jia, J., Bechtel, A., Liu, Z., Strobl, S., Sun, P., Sachsenhofer, R.F., 2013. Oil shale formation in the Upper Cretaceous Nenjiang Formation of the Songliao Basin (NE China): implications from organic and inorganic geochemical analyses. Int. J. Coal Geol. 113, 11–26. https://doi.org/10.1016/j.coal.2013.03.004.
- Johns, W.D., McKallip, T.E., 1989. Burial diagenesis and specific catalytic activity of illite-smectite clays from Vienna Basin, Austria. AAPG Bull. 73, 472–482. https://doi.org/10.1016/0378-7788(89)90007-8.
- Katz, B.J., Arango, 2018. Organic porosity: a geochemist's view of the current state of understanding. Org. Geochem. 123, 1–16. https://doi.org/10.1016/ j.orggeochem.2018.05.015.
- Kleber, M., Bourg, I.C., Coward, E.K., Hansel, C.M., Myneni, S.B., Nunan, N., 2021. Dynamic interactions at the mineral—organic matter interface. Nat. Rev. Earth Environ. 2, 402–421. https://doi.org/10.1038/s43017-021-00162-y.
- Ko, L.T., Ruppel, S.C., Loucks, R.G., Hackley, P.C., Zhang, T., Shao, D., 2016. Pore and pore network evolution of upper cretaceous boquillas (Eagle Ford-Equivalent) mudrocks: results from gold tube pyrolysis experiments. AAPG Bull. 100, 1693–1722. https://doi.org/10.1306/04151615092.
- Lewan, M.D., 1997. Experiments on the role of water in petroleum formation. Geochem. Cosmochim. Acta 61, 3691–3723. https://doi.org/10.1016/S0016-7037(97)00176-2.
- Li, H.B., Wu, Z.C., Zhang, M., Jin, X.L., Tian, X.M., 2023. The geochemical characteristics and migration-accumulation significances of shale oil in Lucaogou Formation of Jimsar Sag. F.B. Oil Gas Field 30 (4), 579–585. https://doi.org/10.6056/dkyqt202304008.
- Liang, C., Cao, Y.C., Liu, K.Y., Jiang, Z.X., Wu, J., Hao, F., 2018. Diagenetic variation at the lamina scale in lacustrine organic-rich shales: implications for hydrocarbon migration and accumulation. Geochem. Cosmochim. Acta 229, 112–128. https:// doi.org/10.1016/j.gca.2018.03.017.
- Liu, B., Mohammadi, M.R., Ma, Z.L., Bai, L.H., Wang, L., Xu, Y.H., Ostadhassan, M., Abdolhossein, H.S., 2023. Evolution of porosity in kerogen type I during hydrous and anhydrous pyrolysis: experimental study, mechanistic understanding, and model development. Fuel 338, 127149. https://doi.org/10.1016/ i.fuel.2022.127149.
- Loucks, R.G., Reed, R.M., 2014. Scanning-electron-microscope petrographic evidence distinguishing organic-matter pores associated with depositional organic matter versus migrated organic matter. GCAGS J. 3, 51–60. https://www.researchgate.net/publication/273258423.

Loucks, R.G., Reed, R.M., Ruppel, S.C., Hammes, U., 2012. Spectrum of pore types and networks in mudrocks and a descriptive classification for matrix-related mudrock pores. AAPG Bull. 96, 1071–1098. https://doi.org/10.1306/08171111061.

- Lu, H., Li, Q., Yue, D.L., Wu, Y., Gao, J., Wu, S.H., Wang, W.R., Li, M., An, K.Q., 2023. Quantitative characterization and formation mechanism of the pore system heterogeneity: examples from organic-rich laminated and organic-poor layered shales of the upper triassic Chang 7 member in the southern Ordos Basin, China. Mar. Petrol. Geol. 147, 105999. https://doi.org/10.1016/ j.marpetgeo.2022.105999.
- Lynch, F.L., 1996. Mineral/water interaction, fluid flow, and Frio sandstone diagenesis Evidence from the rocks. AAPG Bull. 80, 486—504.
- Mastalerz, M., Schimmelmann, A., Drobniak, A., Chen, Y., 2013. Porosity of Devonian and Mississippian New Albany Shale across a maturation gradient: insights from organic petrology, gas adsorption, and mercury intrusion. AAPG Bull. 97, 1621–1643. https://doi.org/10.1306/04011312194.
- Mayer, L.M., 1994. Surface area control of organic carbon accumulation in continental shelf sediments. Geochem. Cosmochim. Acta 58, 1271–1284.
- Mei, Q.L., Guo, R.L., Zhou, X.P., Cheng, G.F., Li, S.X., Bai, Y.B., Liu, J.Y., Wu, W.T., Zhao, J.Z., 2023. Pore structure characteristics and impact factors of laminated shale oil reservoir in Chang 73 sub-member of Ordos Basin, China. NGGS 8, 227–243. https://doi.org/10.1016/j.jnggs.2023.07.003.
- Milliken, K.L., 2003. Late diagenesis and mass transfer in sandstone shale sequences. Treat. Geochem. 7, 159–190. https://doi.org/10.1016/B0-08-043751-6/07091-2
- Milliken, K.L., Esch, W.L., Reed, R.M., Zhang, T., 2012. Grain assemblages and strong diagenetic overprinting in siliceous mudrocks, Barnett shale (Mississippian), fort worth basin, Texas. AAPG Bull. 96, 1553–1578. https://doi.org/10.1306/ 12011111129
- Milliken, K.L., Rudnicki, M., Awwiller, D.N., Zhang, T., 2013. Organic matter-hosted pore system, Marcellus formation (Devonian), Pennsylvania. AAPG Bull. 97, 177–200. https://doi.org/10.1306/07231212048.
- Pan, C.C., Jiang, L.L., Liu, J.Z., Zhang, S.C., Zhu, G.Y., 2010. The effects of calcite and montmorillonite on oil cracking in confined pyrolysis experiments. Org. Geochem. 41, 611–626. https://doi.org/10.1016/j.orggeochem.2010.04.011.
- Pommer, M., Milliken, K., 2015. Pore types and pore-size distributions across thermal maturity, Eagle Ford Formation, southern Texas. AAPG Bull. 99, 1713–1744. https://doi.org/10.1306/03051514151.
- Rickard, D., 2007. 3rd GW Luther, Chemistry of iron sulfides. Chem. Rev. 107, 514–562.
- Shan, C.A., Shi, Y.K., Liang, X., Zhang, L., Wang, G.C., Jiang, L.W., Zou, C., He, F.Y., Mei, J., 2024. Diagenetic characteristics and microscopic pore evolution of deep shale gas reservoirs in Longmaxi Formation, Southeastern Sichuan basin, China. Unconv. Res. 4, 100090. https://doi.org/10.1016/j.uncres.2024.100090.
- Sing, K.S.W., 1985. Reporting physisorption data for gas solid systems with special reference to the determination of surface area and porosity (Recommendations 1984). Pure Appl. Chem. 57, 603–619. https://doi.org/10.1351/pac198557040603.
- Smith, J.T., Ehrenberg, S.N., 1989. Correlation of carbon dioxide abundance with temperature in clastic hydrocarbon reservoirs: relationship to inorganic chemical equilibrium. Mar. Petrol. Geol. 6, 129–135. https://doi.org/10.1016/0264-8172(89)90016-0.
- Sun, L., Fu, D., Wu, Y., Wang, Z.X., 2022. The current study and development of organic-matter pores in organic-rich shale. Arabian J. Geosci. 15, 62. https:// doi.org/10.1007/s12517-021-09384-2.
- Sweeney, J.J., Burnham, A.K., 1990. Evaluation of a simple model of vitrinite reflectance based on chemical kinetics. A APG Bull. 74, 1559–1570. https://doi.org/10.1306/0C9B251F-1710-11D7-8645000102C1865D.
- Tannenbaum, E., Kaplan, I.R., 1985a. Low-molecular weight hydrocarbons generated during hydrous and dry pyrolysis of kerogen. Nature 317, 708–709. https:// doi.org/10.1038/317708a0.
- Tannenbaum, E., Kaplan, I.R., 1985b. Role of minerals in the thermal alteration of organic matter-I: generation of gases and condensates under dry condition. Geochem. Cosmochim. Acta 49, 2589–2604. https://doi.org/10.1306/94886a92-1704-11d7-8645000102c1865d.
- Tannenbaum, E., Huizinga, B.J., Kaplan, I.R., 1986. Role of minerals in thermal alteration of organic matter II: A material balance. AAPG Bull. 70, 1156—1165. https://doi.org/10.1111/J.1945-5100.2007.TB00569.X.
- Tissot, B.P., Welte, D.H., 1984. Petroleum Formation and Occurrence, second ed. Springer-Verlag, Berlin.
- Wang, L., Guan, X.D., Wang, J.Y., Sun, Z.Y., Xu, H.Y., 2023. Characteristics and controlling factors of the upper permian dalong Formation in northwestern Sichuan Basin, China. Front. Earth Sci. 10. https://doi.org/10.3389/feart.2022.1024357.
- Wang, D.X., Hu, H.Y., Wang, T., Tang, T., Li, W.P., Zhu, G.G., Chen, X.Y., 2024. Difference between of coal and shale pore structural characters based on gas adsorption experiment and multifractal analysis. Fuel 371, 132044. https://doi.org/10.1016/j.fuel.2024.132044.
- Waples, D.W., 2000. The kinetics of in-reservoir oil destruction and gas formation: constraints from experimental and empirical data and from thermodynamics. Org. Geochem. 31, 553–575. https://doi.org/10.1016/S0146-6380(00)00023-1.
- Xiao, Q.L., Sun, Y.G., Chai, P.X., 2011. Experimental study of the effects of thermochemical sulfate reduction on low molecular weight hydrocarbons in confined systems and its geochemical implications. Org. Geochem. 42, 1375–1393. https://doi.org/10.1016/j.orggeochem.2011.08.014.
- Xiao, Q.L., Amrani, A., Sun, Y.G., He, S., Cai, C.F., Liu, J.Z., Said-Ahmad, W., Zhu, C.S.,

- Chen, Z.L., 2018. The effects of selected minerals on laboratory simulated thermochemical sulfate reduction. Org. Geochem. 122, 41–51. https://doi.org/10.1016/j.orggeochem.2018.04.004.
- Xiao, Q.L., Sun, Y.G., He, S., Liu, J.Z., Zhu, C.S., 2019. Thermal stability of 2-thiadiamondoids determined by pyrolysis experiments in a closed system and its geochemical implications. Org. Geochem. 130, 14–21. https://doi.org/10.1016/j.orggeochem.2019.02.003.
- Xiao, Q.L., Liu, A., Li, C.X., Chen, Q., Jiang, X.C., Cai, S.Y., 2020. Formation and evolution of nanopores in highly matured shales at OverMature stage: insights from the hydrous pyrolysis experiments on cambrain shuijintuo shale from the middle yangtze region. Earth Sci. 45 (6), 2160–2171. https://doi.org/10.3799/dqlxx.2019.248 (in Chinese).
- Xin, B.X., Zhao, X.Z., Hao, F., Jin, F.M., Pu, X.G., Han, W.Z., Xu, Q.L., Guo, P.F., Tian, J.Q., 2022. Laminae characteristics of lacustrine shales from the Paleogene Kongdian Formation in the Cangdong Sag, Bohai Bay Basin, China: Why do laminated shales have better reservoir physical properties. Int. J. Coal Geol. 26, 104056. https://doi.org/10.1016/j.coal.2022.104056.
- Xiong, Y., Jiang, W., Wang, X., Li, Y., Chen, Y., Zhang, L., Lei, R., Peng, P., 2016. Formation and evolution of solid bitumen during oil cracking. Mar. Petrol. Geol. 78, 70–75. https://doi.org/10.1016/j.marpetgeo.2016.09.008.

- Yang, S., Chen, G., Lv, C., Li, C., Yin, N., Yang, F., Xue, L., 2018. Evolution of nanopore structure in lacustrine organic-rich shales during thermal maturation from hydrous pyrolysis, minhe basin, northwest China. Energy Explor. Exploit. 36 (2), 265–281. https://doi.org/10.1177/0144598717723647.
- Zhang, S.M., Yang, Y.M., Hong, H.T., et al., 2022. Reservoir characteristics and its petroleum significance of Jurassic Da'anzhai shale interval in central Sichuan Basin, SW China. J. China Univ. Min. Technol. 51 (4), 718–730 (in Chinese).
- Zhang, S., Su, L., Zhang, D., Yang, H.Z., Kang, Q.Q., 2023. Hydrocarbon generation and expulsion process in the deepwater area of the Qiongdongnan Basin of China: insights from artificial thermal maturation experiments. J. Pet. Explor. Prod. Technol. 13, 427–438. https://doi.org/10.1007/s13202-022-01558-2.
- Zhang, S.C., Zhang, B., Wang, X.M., Feng, Z.H., He, K., Wang, H.J., Fu, X.L., Liu, Y.K., Yang, C.L., 2023. Gulong shale oil enrichment mechanism and orderly distribution of conventional—unconventional oil in the Cretaceous Qingshankou Formation, Songliao Basin, NE China. Petrol. Explor. Dev. 50, 911–923.
- Zheng, Y., Liao, Y.H., Wang, J., Xiong, Y.Q., Wang, Y.P., Peng, P.A., 2024. Factors controlling the heterogeneity of shale pore structure and shale gas production of the Wufeng-Longmaxi shales in the Dingshan plunging anticline of the Sichuan Basin, China. Int. J. Coal Geol. 282, 104434. https://doi.org/10.1016/j.coal.2023.104434.